

# Dissertation

submitted to the  
Combined Faculties for the Natural Sciences and for Mathematics  
of the Ruperto-Carola University of Heidelberg, Germany  
for the degree of  
Doctor of Natural Sciences

presented by  
Diplom-Physiker Robert R. Kellner  
born in Bayreuth

Oral examination: June 20th, 2007

# STED microscopy with Q-switched microchip lasers

Referees: Prof. Dr. Stefan W. Hell  
Prof. Dr. Josef Bille

## Zusammenfassung

Das Lichtmikroskop ist ein wertvolles wissenschaftliches Instrument in der modernen Biowissenschaft, trotzdem war sein volles Potential durch die beugungsbegrenzte Auflösung eingeschränkt. Ein Konzept, welches einen sättigbaren optischen Übergang fluoreszenter Moleküle, nämlich stimulierte Emission (*stimulated emission depletion*, STED) ausnutzt, ermöglicht es, diese Begrenzung zu überwinden und bietet eine nicht mehr durch Beugung begrenzte Auflösung. In dieser Arbeit wird die STED Mikroskopie als Hilfsmittel in der Zellbiologie weiter etabliert, indem Ring-ähnliche Strukturen des Proteins Bruchpilot in neuromuskulären Verbindungen in *Drosophila* Larven, sowie das Aggregationsverhalten des nikotinischen Acetylcholin-Rezeptors in Säugerzellen aufgedeckt werden. Darüber hinaus wird die Leistungsfähigkeit von STED Mikroskopen weiter verbessert, indem das Bleichverhalten fluoreszierender Farbstoffe untersucht wird. Aus diesen Ergebnissen wird ein neues Beleuchtungsschema für geringeres Photobleichen und erhöhtes Signal entwickelt. Zum ersten mal wird eine neue Herangehensweise an die STED-Mikroskopie mit einem gütegeschalteten (*Q-switched*) Mikrochip-laser, welcher Titan-Saphir basierende Lasersysteme ersetzt, erfolgreich umgesetzt. Die Anwendbarkeit dieses neuen Ansatzes und eine über die Beugungsgrenze hinaus erhöhte Auflösung von unter 25 nm wird an kolloidalen Nanopartikeln und in biologischen Proben demonstriert. Die Auswahl anwendbare Farbstoffe für die STED-Mikroskopie wird weiter in den blauen Bereich ausgedehnt und eröffnet dadurch neue Anwendungsmöglichkeiten.

## Abstract

The far-field light microscope is a valuable scientific instrument in modern life sciences, nevertheless, its full potential was constrained by the diffraction-limited resolution. A concept exploiting a saturable optical transition of fluorescent molecules, namely stimulated emission depletion (STED), allowed to overcome this restriction and provides diffraction-unlimited resolution in far-field light microscopy.

In this thesis STED microscopy as a tool in cell biology is further established by revealing the ring-like structure of the Bruchpilot protein in larval *Drosophila* neuromuscular junctions and clustering behavior of the nicotinic acetylcholine receptor in mammalian cells. Moreover, the performance of STED microscopes is further improved by examining photobleaching behavior of fluorescent dyes and presenting a new illumination scheme for reduced photobleaching and increased signal. For the first time a new approach to STED microscopy with a Q-switched microchip laser, replacing a Ti:Sapphire-based laser system, was successfully implemented. The applicability of this approach and an increase in resolution beyond the diffraction limit to below 25 nm is demonstrated with colloidal nanoparticles and in biological samples. The range of applicable dyes for STED microscopy is further extended into the blue regime, widening the field of possible applications.

# Contents

<b>1</b>	<b>Introduction</b>	<b>1</b>
1.1	Microscopy in cell biology . . . . .	1
1.2	Modern light microscopy . . . . .	2
1.2.1	Special imaging modes . . . . .	2
1.2.2	Novel light microscopy techniques . . . . .	2
1.3	Towards nanoscale resolution in far-field light microscopy . . . . .	3
1.3.1	The resolution issue . . . . .	4
1.3.2	Overcoming the barrier . . . . .	5
<b>2</b>	<b>Advances in STED microscopy</b>	<b>8</b>
2.1	The STED Setup . . . . .	8
2.2	PSF engineering for STED microscopy . . . . .	10
2.3	Spectral characterization of suitable STED-dyes . . . . .	11
2.4	Examining photobleaching . . . . .	12
2.4.1	Signal increase in standard confocal microscopy . . . . .	13
2.4.2	Predominant bleaching pathways in STED microscopy . . . . .	16
2.5	STED applications in cell biology . . . . .	18
2.5.1	STED microscopy reveals ring-like structures in <i>Drosophila</i> NMJ . . . . .	19
2.5.2	STED microscopy for investigation of acetylcholine receptors . . . . .	22
<b>3</b>	<b>STED microscopy with Q-switched microchip lasers</b>	<b>28</b>
3.1	The shift to Q-switched microchip lasers . . . . .	28
3.1.1	A new approach with Q-switched microchip lasers . . . . .	28
3.1.2	Blue dyes for STED microscopy . . . . .	29
3.2	The STED setup using Q-switched microchip lasers . . . . .	30
3.2.1	Pulse timing and beam shaping . . . . .	31
3.2.2	Increasing the speed of Q-switched microchip laser STED microscopy . . . . .	32
3.2.3	The final setup . . . . .	33
3.3	Sub-diffraction resolution demonstrated . . . . .	34
<b>4</b>	<b>Conclusion and outlook</b>	<b>37</b>
	<b>Bibliography</b>	<b>39</b>

---

<b>A Appendix</b>	<b>46</b>
A.1 Imaging acetylcholine receptors . . . . .	46
A.1.1 Cell culture . . . . .	46
A.1.2 Preparation of single plasma membrane sheets . . . . .	46
A.1.3 Cholesterol depletion of cells and single plasma membrane sheets . . . . .	46
A.2 Miscellaneous . . . . .	46
A.2.1 PtK2 cell preparation for bleaching experiments . . . . .	46
A.2.2 Mowiol . . . . .	46
A.2.3 Preparation of fluorescent nanoparticles . . . . .	47
<b>List of publications</b>	<b>49</b>

# Abbreviations

2D	two-dimensional
3D	three-dimensional
AChR	acetylcholine receptor
AFM	atomic force microscope
APD	avalanche photodiode
BRP	Bruchpilot
CARS	coherent anti-Stokes Raman-scattering
CSR	complete spatial randomness
CDx	methyl- $\beta$ -cyclodextrin
CI	confidence interval
CLSM	confocal laser scanning microscope
FLIM	fluorescence lifetime imaging
FRAP	fluorescence recovery after photobleaching
FRET	Förster resonance energy transfer
FWHM	full-width half-maximum
NMJ	neuromuscular junction
OPA	optical parametric amplifier
OPO	optical parametric oscillator
PBS	polarizing beam-splitter
PCF	photonic crystal fiber
PSF	point spread function
PVA	poly(vinyl alcohol)
RegA	regenerative amplifier
RESOLFT	reversible saturable optical (fluorescent) transition
SEM	scanning electron microscope
SNOM	scanning near-field optical microscope
SLM	spatial light modulator
STED	stimulated emission depletion
STM	scanning tunneling microscope
TEM	transmission electron microscope
Ti:Sapphire	titanium-sapphire
VLP	virus-like particle

# 1 Introduction

## 1.1 Microscopy in cell biology

When Robert Hooke used a microscope in 1664 to observe “minute objects” [1] he used the focused light of an oil lamp to illuminate his samples. Differences in reflectivity and in the refractive index within the investigated structure allowed him to distinguish small features. In his work, Hooke coined the term “cell” and presented the first graphical representation of microscopic objects.

Over the next centuries, light microscopes were improved and have become an important tool for scientists from different fields. In 1873, Ernst Abbe discovered that the resolution of a far-field light microscope is essentially limited by diffraction to slightly less than half the wavelength of the imaging light [2].

To circumvent this barrier, new types of microscopes that do not utilize light to generate images have emerged over the last decades. The development of geometric electron optics [3, 4] and the transmission electron microscope (TEM) in 1932 [5] opened up new possibilities, especially in cell biology. The scanning electron microscope (SEM) was derived just a few years later. Modern TEMs can image with a resolution of close to or below 0.1 nm [6]. Unfortunately, the high energy electron beams used in these microscopes are destructive for biological material. Moreover, the samples under investigation must be fixed, embedded in epoxy or frozen and imaged under vacuum conditions. These restrictions make electron microscopy incompatible with live-cell imaging.

Scanning probe microscopy techniques, like atomic force microscopy (AFM), scanning tunneling microscopy (STM), and scanning near-field optical microscopy (SNOM) also provide the possibility to image samples at the atomic scale. Especially AFM and SNOM are able to image small details of biological specimen and have proven valuable for cell biology [7]. However, scanning probe microscopy is inherently surface bound and therefore incapable of three-dimensional (3D) or intracellular imaging.

Far-field light microscopy has thus remained the most useful and versatile technique for cell biologists. Over time, more sophisticated methods to obtain higher contrast were required. For example, the dark field method introduced by Siedentopf and Zsigmondy [8] in 1902 and the phase contrast method developed by Zernike [9, 10] in 1934 widened the field of applications. The introduction of fluorescent markers, that allow labeling with very high specificity and high contrast imaging has led to the development of various new imaging methods. These methods are the subject of the next section.

## 1.2 Modern light microscopy

The development of fluorescence microscopy gave biologists a versatile tool to investigate various processes in living cells. Imaging fluorescently labeled samples against an otherwise dark background results in high contrast images. Nowadays, a wide variety of fluorescent markers covers the whole visible spectrum and several differently labeled features can be imaged simultaneously. Some special techniques that utilize the unique properties of fluorescent molecules will be described briefly in the following paragraphs.

### 1.2.1 Special imaging modes

The lifetime of a fluorescent molecule is usually dependent on the chemical environment. Therefore, by taking an image, where the average fluorescence lifetime for each spatially resolved element is measured, other physiological parameters, like pH or  $\text{Ca}^{2+}$  concentration, can be spatially resolved. A good review of this method, called fluorescence lifetime imaging microscopy (FLIM) is given in Ref. [11].

FLIM can also be used to determine small separation distances between two fluorescent molecules: Non-radiative energy transfer between an excited donor molecule to an acceptor molecule via dipole-dipole coupling can occur. This phenomenon, known as Förster resonance energy transfer (FRET), can take place if there is a spectral overlap between the acceptor and the donor molecule. The transfer varies with the sixth power of the separation distance between the two molecules involved [12]. The accompanying change in fluorescence lifetime as observed with FLIM, or the change in the emission spectrum, can be detected and used to determine molecular conformation, association and separation in the range of 1–10 nm [13].

It is also possible to study dynamic transport processes using fluorescent markers. For example, the photobleaching of fluorophores is exploited in fluorescence recovery after photobleaching (FRAP) measurements. For this method, a certain area of the cell is photobleached with a high-intensity laser. If unbleached neighboring molecules diffuse into the bleached regions, the recovery of fluorescence can be monitored over time. This way, the mobility in cellular compartments and tissues or binding studies can be performed [14]. In FRAP experiments with fluorescent proteins that are expressed by the cell, the expression and distribution of the protein can be monitored [15]. Similar studies can be performed with photoswitchable proteins [16], where fluorescent markers can be selectively switched into a dark or a fluorescent state.

### 1.2.2 Novel light microscopy techniques

With the availability of laser light sources over a wide wavelength range and with sufficient intensity, novel microscopy techniques have been invented. Since biological cells are three dimensional objects, a microscope with optical sectioning capability is of great interest. Consequently, several concepts have emerged for 3D imaging of cells.

For example, the confocal microscope allows high resolution imaging of translucent objects with reduced out-of-focus blur [17]. This is accomplished by imaging a point like light source

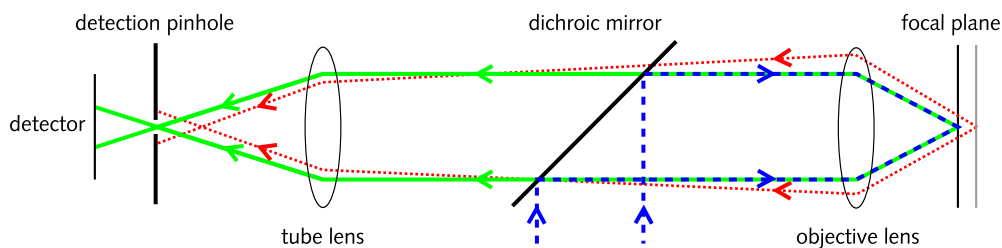


**Figure 1.1:** The working principle of a confocal microscope: the light from a point-like illumination source (blue) is imaged as a diffraction-limited spot into the sample. The light emanating from the sample (green) is collected and imaged onto a detection pinhole. Most of the unwanted out of focus light (red) is rejected by the pinhole.

into the sample and by using a detection pinhole that rejects light not emanating from the focus of the illuminated sample (see Fig. 1.1). In order to acquire an image, the sample has to be moved through the focal spot and the fluorescence is recorded. With the introduction of the confocal laser scanning microscope (CLSM), where the laser beam instead of the sample is moved, faster acquisition times have been realized [18].

Another very successful approach to optical sectioning is based on multi-photon absorption of fluorescent molecules [19]. Usually, a molecule is excited by absorbing one photon with sufficient energy to overcome the energy difference between the ground state and an excited state of the molecule. This can also be achieved by the combined absorption of two or more photons of lower energy, if the total energy of these photons is sufficient for the excitation process. Such a process requires a very high photon density in order to be effective. For example, in two-photon excitation the excitation probability depends quadratically on the applied intensity. Therefore efficient excitation takes place only in the very center of the focused beam and a detection pinhole is not required for optical sectioning. The two-photon excitation wavelength is usually in the near infrared spectrum, where absorption and scattering processes of biological specimen is very low. Two- and multiphoton excitation is therefore ideally suited for deep tissue imaging [20], but no resolution improvement is gained due to the application of longer wavelengths.

Other nonlinear multiphoton imaging techniques include coherent anti-Stokes Raman-scattering (CARS) microscopy and second or third harmonic generation microscopy [21]. These methods allow high contrast imaging of the samples without the need for a contrast enhancing label. The different light microscopy techniques can be combined with the various imaging modes described before and open a wide variety of applications.

### 1.3 Towards nanoscale resolution in far-field light microscopy

The resolution capability of a microscope is its ability to separate two objects, that are close to each other. In 1873, Ernst Abbe published the first detailed investigation of the resolution capability

of a far-field light microscope [2]. He concluded that the resolution is limited by diffraction to approximately  $\lambda/(2n \sin \alpha) = \lambda/(2NA)$ , with  $\lambda$  denoting the wavelength of the light used in the image formation process,  $n$  the refractive index,  $\alpha$  the semi-aperture angle and  $NA$  the numerical aperture of the objective lens.

### 1.3.1 The resolution issue

In a far-field spot-scanning light microscope the resolution is limited by the form and the extent of the intensity distribution  $h(\mathbf{r})$  of the focal spot, commonly referred to as the point spread function (PSF). In such a microscope, the image is formed by scanning the focal spot over the sample, and detecting the excited fluorescence. The image is therefore a convolution of an object with the PSF:

$$I = h \otimes G \quad (1.1)$$

Here,  $I$  and  $G$  denote the image and the object, respectively. This implies that a recorded object is broadened and that an infinitely small object would create a spreaded image resembling the PSF. In a conventional focusing light microscope, the PSF can be described by Bessel functions and the lateral distance between the first two minima is given by:

$$\Delta x, \Delta y = 1.22 \frac{\lambda}{NA} \quad (1.2)$$

In the axial direction, the PSF is elongated and the distance between the two first minima is given by [22]:

$$\Delta z = 4.00 \frac{n\lambda}{NA^2} \quad (1.3)$$

With unaberrated single peak PSFs, the intensity distribution can be well approximated by a Gaussian distribution and the Rayleigh criterion for resolution can be applied. The Rayleigh criterion specifies that two particles that are close to each other can be distinguished if their separation is larger than the full-width half-maximum (FWHM) of the PSF. Evidently, one way to increase the resolution is to narrow down the extent of the PSF of the microscope.

From Eqs. (1.2) and (1.3) it follows, that the spot size can be reduced by decreasing the wavelength and increasing the numerical aperture. However, the wavelength should not be reduced below 365 nm, because shorter wavelengths are harmful to biological tissue and therefore not applicable in live cell imaging [23]. Also, the numerical aperture of an objective lens is technically limited by the largest attainable semi-aperture angles of around 70°. However, the effective numerical aperture can be increased by adding an additional, opposing lens for illumination and detection. This is accomplished in the 4Pi microscope [24], leading to an increased axial resolution of less than 100 nm [25].

In the best case, today's established far-field microscopes with one objective lens achieve a lateral resolution of 180 nm, and 500-800 nm along the optical axis [26]. All technical attempts to improve the resolution remained ultimately constrained by diffraction. Therefore new physical methods needed to be developed.

### 1.3.2 Overcoming the barrier

In the past years, new methods have emerged aiming to improve the resolution of far-field microscopes and eventually overcoming the diffraction barrier altogether. Two fundamentally different concepts underly these methods: one is based on localization, the other on saturable optical transitions.

#### Improved resolution with localization

The development of sophisticated detectors, stable fluorescent dyes and a variety of laser sources made the detection of single fluorescent emitters possible [27]. Although the image of such an emitter is a much larger, diffraction-limited spot, its center can be determined with high accuracy. It has been shown, that a localization of single fluorescent molecules within less than 2 nm is possible [28].

Several new methods have exploited high localization accuracy to obtain high resolution images by ensuring that only a very small fraction of fluorescent markers attached to an object of interest is able to emit within a certain time interval. By taking successive images of single isolated emitters, the localization of each emitter can be performed and an overall image is constructed from the emitters' coordinates.

This method can be implemented by either using photoactivatable fluorescent proteins that are bleached in the course of image acquisition [29], photoswitchable proteins [30] or diffusing labels with binding-specific fluorescence [31]. Albeit having reported a resolution of around 20 nm, these methods require recording times often exceeding several hours and direct imaging without postprocessing is not possible. Also, these methods were so far applied successfully only with total internal reflection excitation and are therefore essentially surface-bound methods.

#### Improved resolution with saturable optical transitions

As outlined in the beginning of this section, in order to substantially improve the resolution of a microscope beyond the diffraction limit, the extent of the PSF must be reduced. This can be achieved with a general concept relying on a saturable transition, namely reversible saturable optical (fluorescent) transition (RESOLFT) [32]. A whole family of methods based on this principle has emerged: stimulated emission depletion (STED) [33], ground state depletion (GSD) [34], and optical switching of fluorescent markers [35].

The underlying idea of these methods can be described by considering a molecule with two arbitrary states, A and B. The transition  $A \rightarrow B$  is induced by light, and no restriction is imposed on the transition  $B \rightarrow A$ . The latter may be spontaneous, but it may also be driven by any other mechanism. The only further assumption is that at least one of these two states is responsible for generating a detectable signal. The feasibility of such a system for generating diffraction-unlimited resolution images in fluorescence microscopy will be exemplified with the STED microscope.

Fig. 1.2 shows the relevant energy levels of a fluorescent molecule and its corresponding A and B states of the RESOLFT concept. The electronic singlet states  $S_0$  (ground state) and  $S_1$  (first excited state) show higher vibrational levels  $S_0^{\text{vib}}$  and  $S_1^{\text{vib}}$ . Higher energy or triplet states are

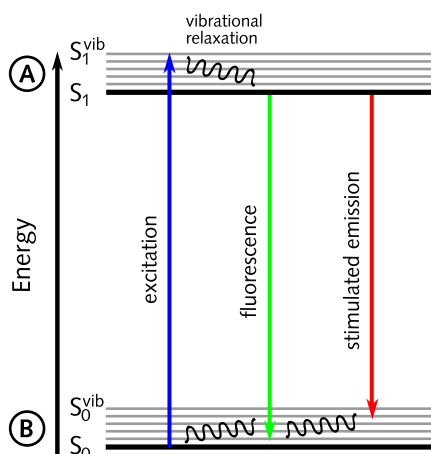


**Figure 1.2:** Relevant singlet energy levels  $S_0$  and  $S_1$  of a fluorescent molecule with superimposed vibrational sublevels  $S_0^{\text{vib}}$  and  $S_1^{\text{vib}}$ . A molecule is excited from the singlet ground state  $S_0$  into higher singlet states  $S_1^{\text{vib}}$ , from where it relaxes to the first excited singlet state  $S_1$ . It can return to the ground state by spontaneous emission of a photon (fluorescence) or by stimulated emission. A and B denote the two different state of the RESOLFT concept.

omitted for the sake of simplicity. According to the Franck-Condon principle such a molecule can be excited from  $S_0$  to one of the higher  $S_1^{\text{vib}}$  states by absorption of a photon with sufficient energy [36]. After vibrational relaxation, the molecule can return to the ground state via the emission of a photon. This transition can either be spontaneous (fluorescence), or induced by another photon (stimulated emission). In a STED microscope, the molecules are excited from the ground state by a short light pulse and a second, red-shifted light pulse (the STED or depletion pulse) is applied to induce stimulated emission of the excited molecules. Since the relaxation from  $S_0^{\text{vib}}$  to  $S_0$  is in the sub-picosecond range and therefore much shorter than the STED pulse, re-excitation after stimulated emission by photons of the same energy can be neglected. Hence, the  $S_1$  state can be depleted and fluorescence is suppressed.

The dynamic interplay of an ensemble of dye molecules relevant for the STED microscope can be mathematically described by a set of coupled differential equations [33]. The rate of fluorescence  $k_{\text{fl}}$  is proportional to the inverse fluorescence lifetime  $1/\tau$ . The rates for the photon induced transitions  $S_0 \rightarrow S_1^{\text{vib}}$  (excitation) and  $S_1 \rightarrow S_0^{\text{vib}}$  (stimulated emission),  $k_{\text{exc}}$  and  $k_{\text{STED}}$ , respectively, are proportional to the photon flux  $h$  and the molecular cross-section  $\sigma$ . The  $S_1$  population  $N_{S_1}$  after an applied STED pulse can be approximated by [37]

$$N_{S_1} \approx N_0 \exp(-\sigma_{\text{STED}} h_{\text{STED}}) = N_0 \eta(h_{\text{STED}}) \quad (1.4)$$

with  $N_0$  denoting the initial  $S_1$  population in the absence of STED. If the PSF of the depletion beam is shaped in a way that it exhibits a local minimum where the intensity is zero, fluorescence is suppressed everywhere except for the zero intensity region. Essentially, with this method the scanning focal spot can be reduced beyond the diffraction limit. Moreover, the strong nonlinear

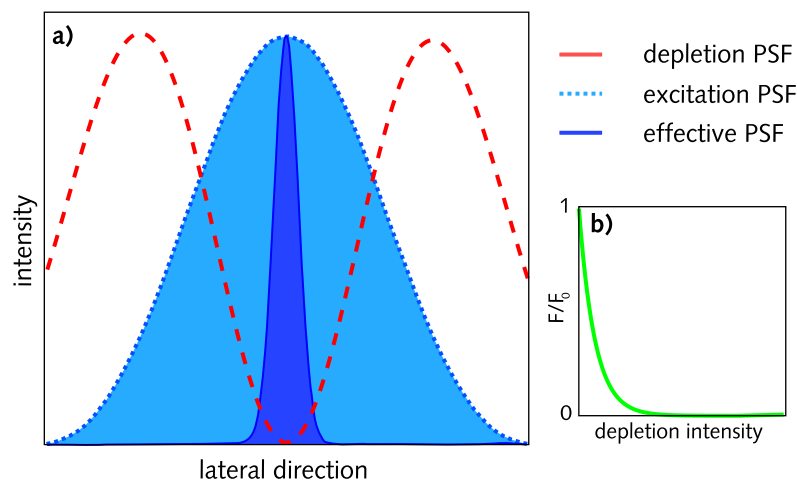


**Figure 1.3:** The resolution limit broken by reversible optical transitions: **a:** Normalized intensity profiles of the excitation and the depletion PSF. The effective PSF is much smaller than the original PSF. **b:** The depletion is strongly dependent on the intensity of the depletion beam.  $F$  denotes the obtained fluorescence signal,  $F_0$  the fluorescence collected when no depletion beam is present.

relationship between residual fluorescence and STED-power from Eq. (1.4) allows the creation of subdiffraction limited focal spots with comparably low light power.

If one defines a saturation intensity  $I_{\text{sat}}$ , at which half of the excited molecules were stimulated to return to the ground state, the resolution of a STED system can be described by [37]:

$$\Delta x = \frac{\lambda}{\pi n \sin \alpha \sqrt{1 + I/I_{\text{sat}}}} \quad (1.5)$$

This shows that with increasing intensity, the resolution can be theoretically narrowed down to the molecular scale. In fact, a lateral resolution of 15–20 nm [38] and an axial resolution of 33 nm [39] was achieved experimentally. With a shift from near infrared dyes to dyes emitting in the yellow-green wavelength range, the first applications of nanoscale STED microscopy to address biological questions were made possible [40, 41].

**This thesis shows** the further optimization of STED microscopy in the visible range and its successful application to cell biology. Furthermore, an analysis of spectral characteristics and bleaching behavior of fluorescent molecules results in a new approach to STED microscopy with compact Q-switched microchip lasers at low repetition rates. The range of dyes viable for STED microscopy is extended further into the blue emission range, and, as a result, STED microscopy can now be used over the whole visible into the near infrared wavelength range, opening new possibilities for multicolor nanoscale resolution imaging.

## 2 Advances in STED microscopy

As outlined in the introduction, the RESOLFT-type STED microscope is a diffraction-unlimited, laser scanning fluorescence microscope. In this chapter the physical and technical details of this concept are further explained and ways to improve the performance of such microscopes are illustrated. Furthermore, applications of STED microscopy in cell biology are presented.

### 2.1 The STED Setup

The STED microscope was implemented by extending a confocal laser scanning microscope with an additional illumination path for fluorescence depletion. Although confocalization is not required for the STED concept, it provides optical sectioning capability and facilitates the comparison between standard confocal and STED resolution. For this work, a flexible STED microscope was built, where a variety of different light sources and beam shaping methods were implemented. This was advantageous for the optimization of the overall performance of STED microscopes and allowed fine-tuning of several relevant physical parameters. A schematic representation of the setup is shown in Fig. 2.1.

The system was built with biological applications in mind. Hence, the microscope is able to utilize fluorescent markers that emit in the visible range. Since the depletion wavelength is commonly chosen at the red end of the dye's emission spectrum [37], a tunable lightsource operating between 500 nm and 650 nm is required. Therefore, an optical parametric oscillator (OPO) (OPO Advanced, APE, Berlin), pumped by a modelocked titanium-sapphire (Ti:Sapphire) laser (MaiTai, Spectra Physics, Mountain View, California) operating at 80 MHz pulse repetition rate was used as the STED light source. The OPO emits femtosecond pulses at the same repetition rate as the pump laser and can be tuned from 530 nm up to 660 nm. The average output power of a well-tuned system can exceed 500 mW in the center of the tuning range, but can drop to less than 150 mW at the tuning edge.

In a previous work [42] it was shown that photobleaching of fluorescent dyes can be reduced if the duration of the STED laser pulses is prolonged to several picoseconds. Accordingly, in this setup the pulses were dispersively stretched by either grating pairs or an 80 m long single-mode fiber. The achieved pulse width ranged between 200 ps and 250 ps, depending on the wavelength and the spectral width of the pulses. In general, using single-mode fibers is favored, because they are easier to handle and readily deliver a high-quality Gaussian beam.

For dye-specific efficient excitation, several pulsed diode lasers at 375 nm, 440 nm, 470 nm, 490 nm and 532 nm were used. These laser diodes can be triggered externally and can operate from single shot up to 80 MHz repetition rate with pulse lengths between 80 ps and 100 ps. With

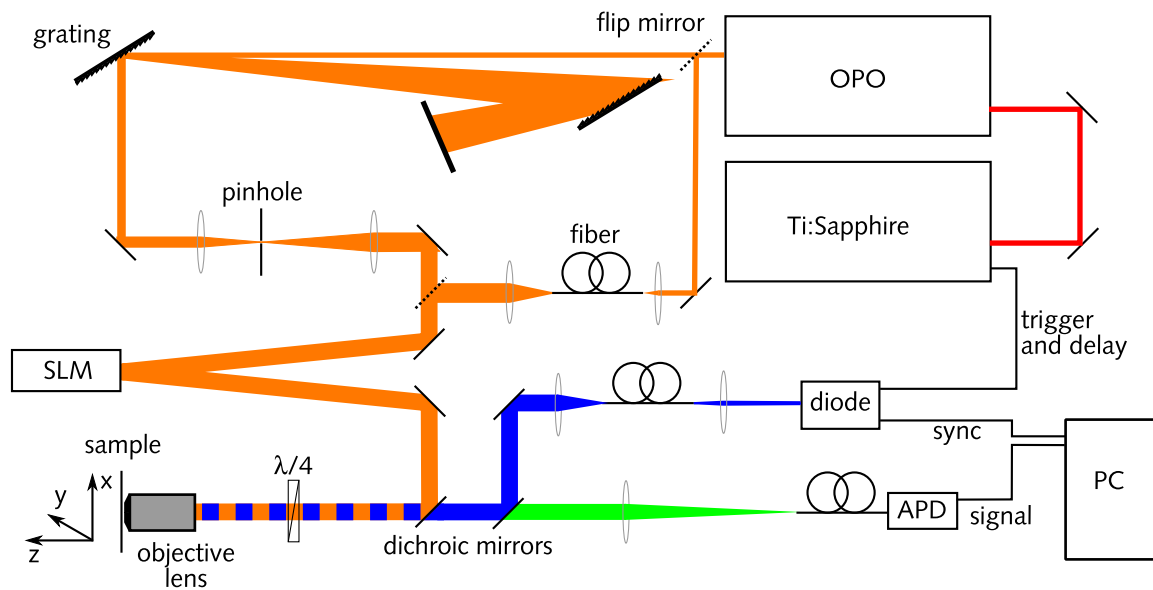


**Figure 2.1:** The light generated by a Ti:Sapphire laser is frequency converted in an optical parametric oscillator (OPO) and the pulses are stretched by either a grating pair or a single-mode fiber. A spatial light modulator (SLM) is used to generate the phase patterns for a zero intensity focal spot. The excitation light sources are fiber coupled laser diodes that can be triggered externally. Both beams are coupled into an objective lens and the fluorescence is collected via the same lens. For confocalization, the fluorescence emanating from the sample is imaged onto a multi-mode fiber and recorded by an avalanche photodiode (APD). The signals are recorded with a computer (PC).

the exception of the 375 nm laser diode, all of these lasers were coupled into single-mode fibers. This way, high-quality single-mode operation was facilitated and switching between different excitation wavelengths could be done very flexibly.

The excitation and the STED beam were coupled into an oil immersion objective lens (HCX PL APO, 100 $\times$ , 1.4 NA, Leica Microsystems, Mannheim, Germany) with appropriate dichroic mirrors. A  $\lambda/4$  plate ensures circular polarization of the beams at the entrance pupil of the objective lens. The fluorescence collected by the same lens was focused with a lens of 400 mm focal length onto a multi-mode fiber (62.5  $\mu\text{m}$   $\varnothing$ ) serving as the confocal pinhole. The core diameter of the fiber corresponds to 71 % of the diameter of the backprojected Airy disc. The fiber was connected to an avalanche photodiode (APD) (SPCM-AQR-13-FC, Perkin Elmer Opto Electronics Europe, Germany) operating in the counting mode, and the generated signal is recorded with a single photon counting module (SPC-730, Becker & Hickl, Berlin, Germany). The timing adjustment of the excitation and the STED pulse was achieved by delaying the synchronization output of the Ti:Sapphire laser as trigger source for the excitation diode with custom made electronics. The image was acquired by piezo-stage scanning of the sample operating in closed loop mode (Nanoblock, Melles Griot, Cambridge, UK). The methods involved in the phase shaping of the STED beam will be explained in the following section.

## 2.2 PSF engineering for STED microscopy

The RESOLFT concept relies on the generation of a PSF with a local minimum of zero intensity. In the past this was mainly achieved by introducing binary phase masks into the STED beam path. Recently, programmable spatial light modulators (SLM), capable of imprinting arbitrary phase patterns onto the STED beam, were also used. Several phase patterns can be employed to generate a feasible STED beam [43], and an overview of optimum patterns and their corresponding PSFs is shown in Fig. 2.2.

Binary phase masks are manufactured by depositing  $\text{MgF}_2$  or cryolite (sodium hexafluoroaluminate,  $\text{Na}_3\text{AlF}_6$ ) onto a flat glass substrate covered by appropriately shaped aluminum masks. Such phase masks can be handled easily and produced with good accuracy. However, they can not be used for complex phase pattern generation and are usually tailored for a specific wavelength.

In order to gain more control over the phase retardation, in this setup a parallel aligned nematic liquid crystal spatial light modulator (Hamamatsu, Hamamatsu City, Japan) was utilized [44]. It is composed of  $1024 \times 768$  pixels that are optically addressed and each pixel can be independently set to a phase retardation of  $0 - 2\pi$ . This way arbitrary phase patterns can be generated over a

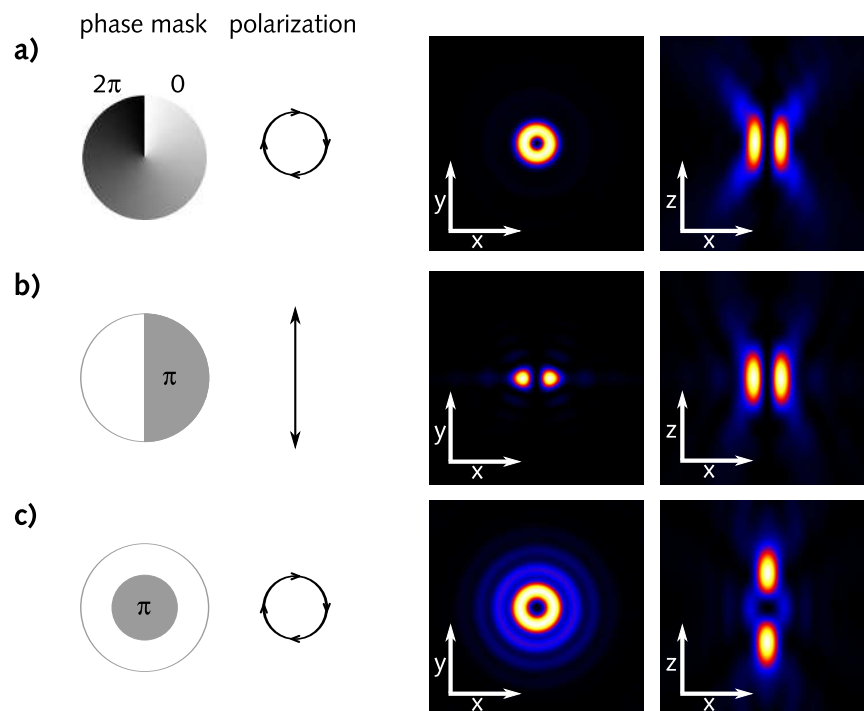


**Figure 2.2:** Different phase retardation masks and their corresponding PSFs calculated for an  $1.4 NA$  oil immersion objective and a wavelength of  $600 \text{ nm}$ . The size of each image is  $3 \mu\text{m} \times 3 \mu\text{m}$ . The two PSFs from **a** and **c** can be combined for an increased 3D resolution. Calculation tools were provided by Dr. Jan Keller, Department of NanoBiophotonics, Max-Planck-Institute for Biophysical Chemistry, Göttingen.

large range of wavelengths. With the SLM it was possible to generate the the helical phase ramp (Fig. 2.2 a) resulting in a donut-shaped PSF well suited for uniform increase in two-dimensional (2D) resolution. Utilizing an SLM is also advantageous for the creation of the mask for increased z-resolution (Fig. 2.2 c), because the diameter of the central phase retardation zone can be controlled online to perfectly match the pupil of the objective lens. An additional feature of the SLM is the extensive ability to correct aberrations of the beam. Such aberrations can be introduced by various optical elements of the microscope or by the investigated specimen itself [45]. Unfortunately, experiments made apparent that some pixels of the SLM showed a wide non-random deviation from their intended phase retardation (data not shown), resulting in imperfections in the PSF. Another drawback of the Hamamatsu SLM is that with increasing light intensity, the readout light tends to alter the phase retardation of the individual pixels and renders the SLM unusable for high-power applications.

## 2.3 Spectral characterization of suitable STED-dyes

In principle, every fluorescent dye can undergo stimulated emission and is therefore applicable for STED microscopy [12]. There is wide variety of fluorescent dyes utilized in fluorescence microscopy today, and the range in which they absorb and emit light exceeds the entire visible spectrum. So far, dyes emitting in the visible range have been seldomly used in STED microscopy and the first applications were using dyes emitting in the near infrared [39]. One aim of this work is to find additional fluorescent markers with their corresponding STED wavelengths for efficient stimulated emission in the whole visible range. The shift from the near infrared to smaller wavelengths would not only result in an increase in resolution, it would also make available more dyes for applications in cell biology. A well suited dye for STED microscopy has on the one hand a depletion curve  $\eta(I)$  showing a very steep decrease with  $I_{\text{sat}}$  being comparably low. On the other hand the residual fluorescence for higher intensities should be negligibly small. The latter is not strictly necessary for improved resolution, it merely means that the confocal background signal is small [37].

Starting from the notion that the stimulated emission cross section of a fluorescence marker approximately follows the corresponding spontaneous emission spectrum, the STED wavelength would be chosen to match the emission maximum. The problem however is, that in this case usually a substantial amount of dye molecules is also re-excited from the ground state by the depletion beam. The task at hand is to find the depletion wavelength showing a high stimulated emission cross section  $\sigma_{\text{STED}}$  and a very low absorption cross section, as illustrated in Fig. 2.3, because the intensity of the depletion beam can be three to four orders of magnitude larger than the excitation intensity. Therefore the STED wavelength is commonly chosen on the red end of the dye's emission spectrum [46].

In this work the behavior of more than 40 different fluorescent dyes was investigated. The depletion curves  $\eta(I)$  at different STED wavelengths as well as the re-excitation by the depletion beam was measured. The bleaching behavior under STED conditions was determined by immobilizing the dye molecules in a poly(vinyl alcohol) (PVA) matrix or by covalently binding single

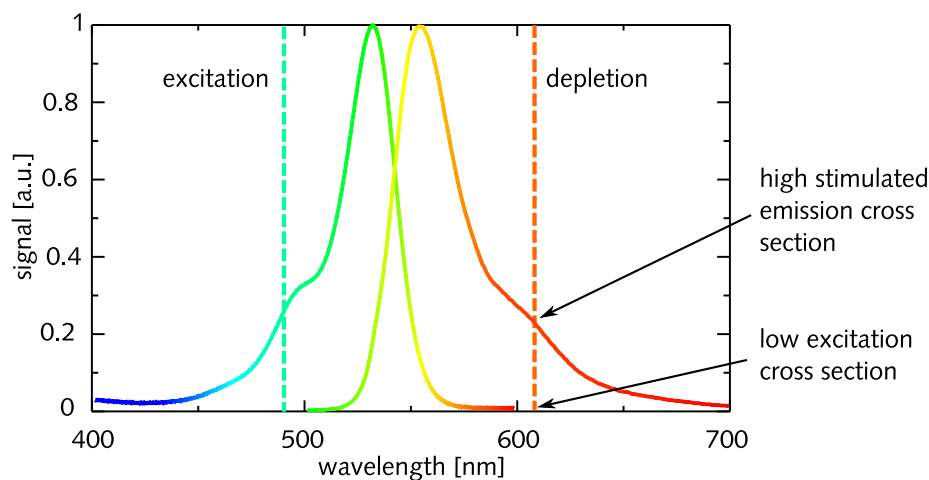


**Figure 2.3:** A typical absorption and emission spectrum of a fluorescent dye (Atto 532, Atto-Tec GmbH, Siegen, Germany). The depletion wavelength is chosen in a way that permits efficient stimulated emission without re-excitation of the dye.

molecules onto a coverslip.

For these measurements, the spatial phase-distribution of the STED beam was not altered and the excitation and STED PSFs were spatially overlapped. The timing of the pulsed laser sources was optimized to achieve maximum stimulated emission. Fast chopping of the STED beam confirmed whether the decrease of fluorescence was immediate and reversible. This way stimulated emission could be discriminated from bleaching effects.

Since the spectral properties and bleaching behavior can be strongly dependent on the environment, extracting quantitative information that can be related to imaging applications is a tedious task. However, it should also be pointed out that all the dyes under investigation showed stimulated emission and are in principle suitable for STED microscopy.

## 2.4 Examining photobleaching

In fluorescence microscopy, as in most other applications, a large signal to noise ratio is beneficial. Therefore, high intensity illumination is applied, often in the form of pulsed laser sources. Apart from that, high illumination intensities are mandatory in multiphoton microscopy [19] and for saturated stimulated emission in STED microscopy. Achieving a large signal to noise ratio is also a challenging predicament in STED microscopy: By increasing the resolution, the focal volume is reduced and consequently the detectable fluorescence is decreased. Accordingly higher excitation intensities or longer acquisition times are required.

Nevertheless, the attainable signal is ultimately limited by photobleaching of the dye. Photobleaching is a dynamic, and in most cases, irreversible process in which molecules lose their ability to fluoresce, because they undergo photoinduced chemical destruction upon absorption of light [47]. Therefore it is important to determine the predominant photobleaching mechanisms and to find strategies to avoid them.

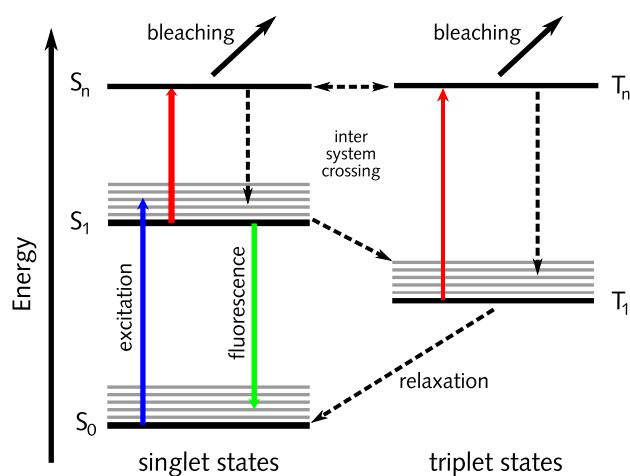


**Figure 2.4:** The different pathways of photobleaching. The molecules can change from the singlet to the triplet states (or vice versa) via intersystem crossing. Absorption from singlet and triplet states into higher excited states can lead to photobleaching.

### 2.4.1 Signal increase in standard confocal microscopy

There are several possibilities for fluorescent molecules to undergo photobleaching [48], and for a better understanding of the bleaching process Fig. 2.4 illustrates the relevant molecular states involved in photobleaching. A fluorophore can be excited from the ground state  $S_0$  into the higher excited singlet state  $S_1$  from where fluorescence or intersystem crossing to the triplet state can occur [12]. The fluorophore may be even further excited into higher singlet or triplet states  $S_n$  or  $T_n$ , respectively. Such excitation processes can again lead to intersystem crossing or even reverse intersystem crossing between both states [49], but unfortunately higher excited state absorption often leads to photobleaching of the dye [50].

Since the  $T_1 \rightarrow T_n$  absorption is often red-shifted with respect to the ground state absorption spectrum [51] and since the triplet lifetime is usually in the range of several microseconds, bleaching or reverse intersystem crossing via the triplet states can be an important factor in STED microscopy. Therefore, in the following the role of bleaching via singlet and triplet states is investigated and a new illumination scheme for reduced photobleaching is presented.

Pulsed light sources for microscopy applications usually work at repetition rates between  $f = 40\text{--}100$  MHz [52], equalling a pulse-to-pulse time  $\Delta t = 1/f$  between 10–25 ns. This is significantly larger than the typical lifetime of the fluorescent state  $S_1$ . Hence, when a dye is illuminated with such a light source, the  $S_1$  state of previously excited molecules is already empty before another pulse arrives, avoiding excitation to  $S_n$  and subsequent bleaching. The triplet state  $T_1$  however, has a lifetime in the microsecond range, thus exceeding  $\Delta t$  by far. This means that, depending on the intersystem crossing rate, a substantial triplet build-up can occur. When molecules are caught in the triplet state they can no longer fluoresce and therefore the average emitted signal of the dye is lowered. A high triplet population can also lead to an increased probability for

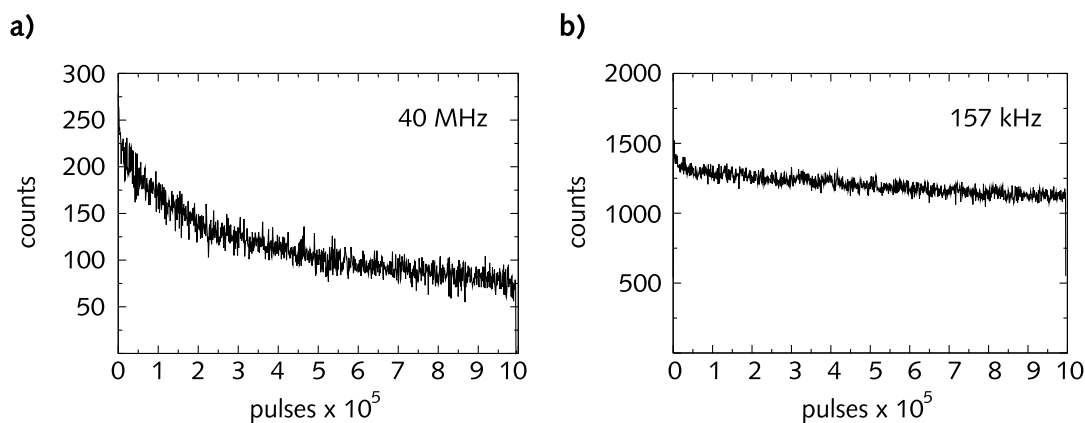


**Figure 2.5:** Fluorescence time-traces per excitation pulses obtained with Rhodamine 6G at 40 MHz (a) and 157 kHz (b). At lower repetition rate the initial signal is not only stronger, photobleaching is also reduced.

bleaching from the triplet state [53].

If the repetition rate of the pulsed lasers is reduced in a way that permits the relaxation of the triplet state  $T_1$  back to the ground state  $S_0$  before the arrival of another light pulse, all unbleached molecules can be excited by subsequent pulses. Moreover, the triplet bleaching channel becomes less important, since  $T_1 \rightarrow T_n$  absorption is reduced due to the lower  $T_1$  population. These effects should not only result in more fluorescence per pulse, but also augment the total signal. The overall image acquisition time however will also increase, because there are less excitation cycles per time interval.

In order to examine this hypotheses experimentally, the two dyes Rhodamine 6G (Lambda Physics, Göttingen, Germany) and Atto 532 (Atto-Tec GmbH, Siegen, Germany) were embedded in PVA and spincoated onto a coverslip. Rhodamine 6G is a well studied dye, where higher excited triplet states were found to be the predominant reactive state for photobleaching [50]. The pulsed excitation diode laser emitting at 470 nm (LDH-P-C-470, Picoquant, Berlin, Germany) can be operated at an arbitrary repetition rate, from single shot up to 80 MHz, which makes it ideal for this experiment.

Fluorescence time-traces were recorded and summed for different excitation repetition rates. The pixel dwell time for each measurement was adjusted such that the fluorescence generated by 1,000 excitation pulses was recorded for each pixel. In order to ensure that the energy of single pulses were the same for all repetition rates, the average power was adjusted accordingly. The resulting signal was measured for several excitation repetition rates, starting off with an average power of  $5 \mu\text{W}$  and a pixel dwell time of 0.025 ms at 40 MHz down to an average power of 19.6 nW and a pixel dwell time of 6.37 ms at 157 kHz. For each repetition rate, four time-traces were recorded and averaged. The difference between the fluorescence behavior is best illustrated by comparing the signals obtained for 40 MHz and 157 kHz repetition rates (see Fig. 2.5).

The total signal obtained during the acquisition time was summed yielding the results displayed in Fig. 2.6 for increasing  $\Delta t = 1/f$ . It becomes evident that with an increasing time difference  $\Delta t$

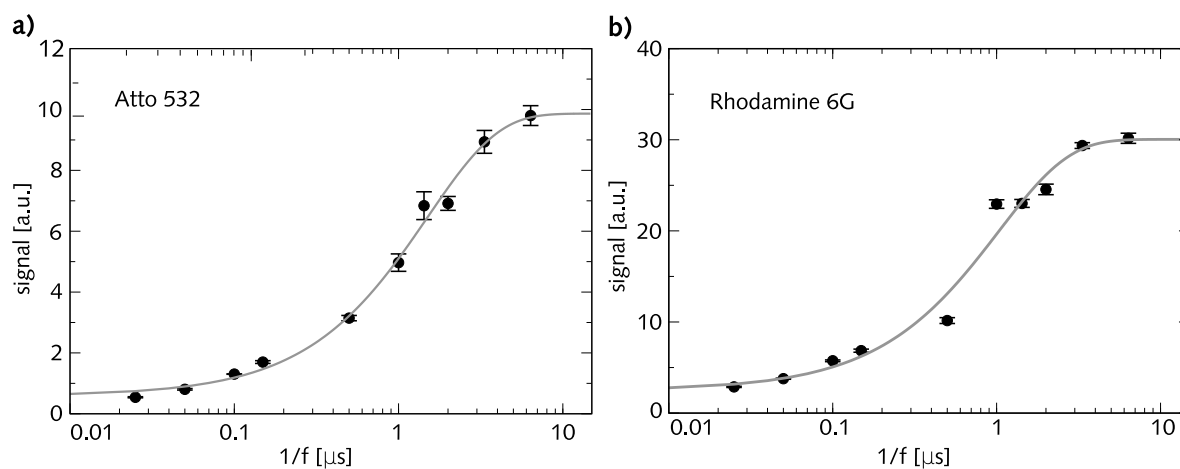


**Figure 2.6:** Fluorescence signal generated for Atto 532 (a) and Rhodamine 6G (b) for a given number of excitation pulses (1,000) per time recording interval. The errors (2–5%) were estimated from the standard deviation of replicate measurements. The solid line represents an exponential fit to the data, resembling the  $1\ \mu\text{s}$  lifetime of the nonfluorescent triplet state.

between subsequent pulses the total number of collected photons, generated by the same number of excitation pulses of equal power is increased. The signal obtained for several different repetition rates fits nicely to an exponential decay of the triplet state with an approximated lifetime of  $1\ \mu\text{s}$ .

These findings show that a major signal increase is gained by decreasing the repetition rate of the excitation laser if the triplet is a major reactive state for photobleaching, or if there is a high intersystem crossing to the triplet state. This effect was further investigated for one- and two-photon excitation and successfully applied to STED microscopy in another work [53, 38].

## 2.4.2 Predominant bleaching pathways in STED microscopy

### Modeling bleaching behavior

In STED microscopy the depletion beam can lead to substantial additional bleaching if the STED wavelength matches the absorption band of  $S_1 \rightarrow S_n$  or  $T_1 \rightarrow T_n$  transitions. The latter is of special importance if the intersystem crossing rate between  $S_1 \rightarrow T_1$  is high.

If STED causes additional bleaching from excited singlet states via  $S_1 \rightarrow S_n$  absorption, the bleaching rate should be dependent on the time delay between the STED and the excitation pulse. If successive images of the same area of a sample are recorded, then the recorded signal  $S$  decreases by a factor  $g$  between  $n$  scans. The decay of  $S$  can accordingly be described by the following equations:

$$\frac{\Delta S}{\Delta n} = -gS \quad (2.1)$$

$$\Rightarrow S(n) = S_0 \exp(-gn) \quad (2.2)$$

with  $S(0) = S_0$ . To account for the fact that there are two different light pulses involved,  $g$  is split up into STED and excitation induced bleaching coefficients:

$$g = g_{\text{STED}} + g_{\text{exc}} \quad (2.3)$$

Assuming further that STED-induced bleaching can happen from the higher excited singlet ( $S_n$ ) and triplet states ( $T_n$ ),  $g_{\text{STED}} = g_{\text{singlet}} + g_{\text{triplet}}$ , the total bleaching coefficient can be written as:

$$g = g_{\text{singlet}} + g_{\text{triplet}} + g_{\text{exc}} \quad (2.4)$$

At repetition rates of 80 MHz, the triplet lifetime is much larger than the time between two laser pulses. Therefore,  $g_{\text{triplet}}$  should be independent of the delay  $\delta$  between the STED and the excitation pulse, and  $g_{\text{singlet}}$  is proportional to the number  $N_1$  of molecules in the short-lived  $S_1$  state. The molecules are excited at  $t = 0$ , and after a delay of  $t = \delta$ , when the STED pulse arrives,  $N_1$  yields

$$N_1(\delta) = N_1(0) \exp(-\delta/\tau) \quad (2.5)$$

with  $\tau$  denoting the fluorescence lifetime of the molecule. Hence,  $g_{\text{singlet}} = g_{\text{singlet}}(\delta)$  and

$$g_{\text{singlet}}(\delta) = g_{\text{singlet}_0} \exp(-\delta/\tau) \quad (2.6)$$

$$\Rightarrow S(n) = S_0 \exp \left[ (g_{\text{singlet}_0} \exp(-\delta/\tau) - g_{\text{triplet}} - g_{\text{exc}}) n \right] \quad (2.7)$$

with  $g_{\text{singlet}_0} = g_{\text{singlet}}(\delta = 0)$ . The excitation bleaching can be determined separately by subsequent scans with no STED beam present. Substituting  $S'_0 = S_0 \exp(-g_{\text{exc}}n)$  and taking the logarithm of both sides of Eq. (2.7) yields:

$$\ln \frac{S(n)}{S'_0} = -(g_{\text{singlet}_0} \exp(-\delta/\tau) + g_{\text{triplet}}) n \quad (2.8)$$

If the dye shows strong STED-induced bleaching via singlet states, determining the delay-dependent bleaching should show an exponential relationship.

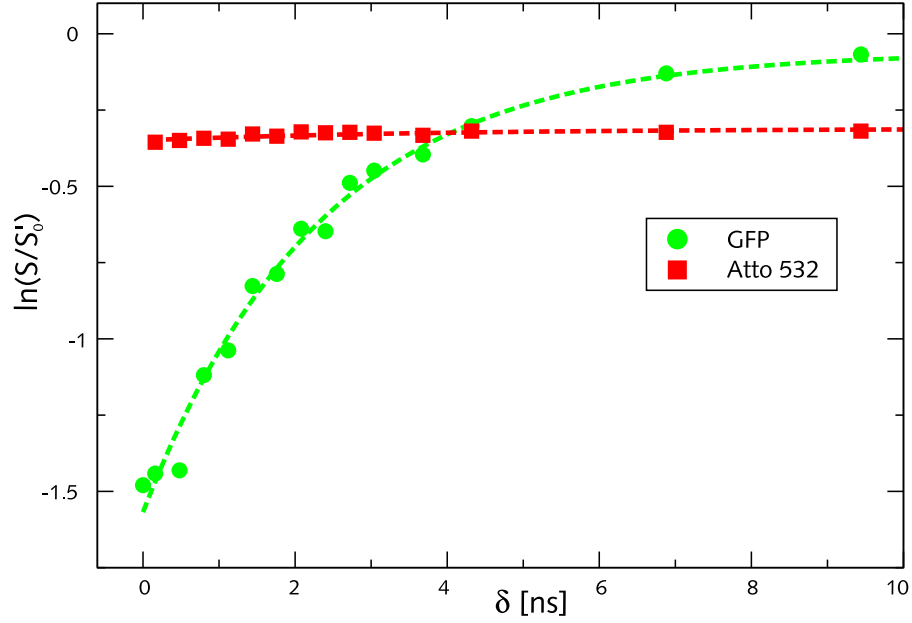


**Figure 2.7:** Bleaching behavior of GFP and Atto 532 with respect to the delay  $\delta$  between the excitation and the STED pulse. While Atto 532 is almost independent of the delay, GFP shows an exponential dependence, corresponding to the fluorescence lifetime of GFP. This indicates that STED-induced bleaching of GFP occurs mainly via the singlet, STED-induced bleaching of Atto 532 via the triplet state.

## Experiments

The difference between singlet and triplet bleaching is exemplified by the following experiment: The fluorescent protein GFP and the Rhodamine-based dye Atto 532 were investigated under STED imaging conditions. GFP was available in the form of spherical, virus-like particles (VLP) containing 120 GFP molecules provided by the laboratory of Jean Cohen, France [54]. For Atto 532 measurements, the PtK2 microtubular network was antibody-labeled with Atto 532 (see Appendix A.2.1). Both samples were mounted in Mowiol (Appendix A.2.2) onto a coverslip. For bleaching under STED imaging conditions, both samples were excited with  $3 \mu\text{W}$  at 490 nm and depleted with 1.3 mW at 570 nm (GFP) and with 13 mW at 615 nm (Atto 532).

The excitation-induced photobleaching factor  $g_{\text{exc}}$  from Eq. (2.2) is determined by taking two subsequent images of the same region with the STED beam blocked. Afterwards, the same region was recorded with both the excitation and the STED beams open, followed by another excitation only image in order to measure the remaining fluorescence. The time delay between the STED and the excitation pulse was varied for a series of measurements using a custom made electronic delay line. This way, a delay dependent bleaching behavior of the dye was determined. The resulting logarithm of the excitation bleaching corrected signals obtained for these two dyes are shown in Fig. 2.7.

The fluorescence lifetimes of the dyes were also determined by time-resolved fluorescence measurements. Eq. (2.8) was fitted to the bleaching measurements to obtain  $g_{\text{singlet}_0}$  and  $g_{\text{triplet}}$ . The

Dye	$\tau/\text{ns}$	$g_{\text{singlet}_0}$	$g_{\text{triplet}}$	$g_{\text{singlet}_0}/g_{\text{triplet}}$
GFP	2.33	1.51	0.06	25.17
Atto 532	3.8	0.04	0.31	0.13

**Table 2.1:** The obtained singlet and triplet bleaching parameters from Eq. (2.8) for GFP and Atto 532.

Atto 532 is bleaching mostly from the triplet state, while GFP is bleaching almost exclusively from the singlet state under STED imaging conditions.

results are shown in Tab. 2.1. The bleaching behavior of Atto 532 is almost independent of the delay between the STED and the excitation pulse. In the case of GFP, however, an exponential dependence corresponding to the fluorescence lifetime is visible. The data suggest that under STED imaging conditions, GFP is prone to bleach from the short-lived singlet state, while Atto 532 bleaches primarily from the long-lived triplet state. In the latter case, reducing the triplet population would also diminish the total bleaching of molecules, which was confirmed experimentally in another work by reducing the repetition rate down to 250 kHz [38]. In order to investigate other multi-step bleaching processes via intermediate singlet and triplet states, repetition rate dependent measurements and sub-picosecond time resolution are required.

Since the singlet state is essential for fluorescence, other options need to be pursued in order to reduce photobleaching from the singlet state. For example, the depletion wavelength can be chosen to cause only minor absorption of molecules in higher singlet states. However, this may counteract efficient stimulated emission leading to a reduced resolution. Other possible methods may be the utilization of protective additives in the sample [55, 56].

## 2.5 STED applications in cell biology

The aim of shifting from near infrared to visible dyes for STED microscopy was to address questions in cell biology with unprecedented resolution. There are only a few dyes emitting in the near infrared that can be utilized as a marker in biological samples, as opposed to the wide varieties of available labels in the visual range. In addition, the smaller wavelengths present a further increase in resolution. From the screening experiments the yellow-green emitting dye Atto 532 turned out to be one of the most promising candidates and was accordingly used for the following studies. In this work, the neuromuscular junction of *Drosophila* and the organization of acetylcholine receptor clusters was studied.

Both studies were performed using the setup described in section 2.1. For the staining of the samples, the dye Atto 532 was conjugated to an anti-mouse IgG (Jackson ImmunoResearch Laboratories, USA) via its succinimidyl ester. Fluorescence excitation was accomplished at 490 nm wavelength with 100 ps pulses from a laser diode (PicoTA 490N, PicoQuant, Berlin, Germany). For STED, the focal excitation spot was overlapped with a donut-shaped spot of 200 ps pulses duration of 615 nm wavelength. The donut shape was generated using a helical phase mask (see Fig 2.2 a) produced by a spatial light modulator (PAL-SLM, Hamamatsu, Hamamatsu City, Japan). The effective PSF of this system was determined experimentally by imaging glass-

adsorbed, point-like primary antibodies stained with Atto 532 labeled secondary antibodies. Lorentzian fits of the intensity profiles revealed a FWHM of  $70.8 \pm 2.3$  nm, which approximately corresponds to the lateral resolution of this setup.

### 2.5.1 STED microscopy reveals ring-like structures in *Drosophila* neuromuscular junctions

#### Introduction

When looking at the processes involved in fast cell-to-cell communication within the nervous system, the synapse is of most interest. In order to uphold fast neurotransmission, the partners involved need to be very close to each other. In addition, on both sides of the synapse, a precise structural arrangement of cellular components is required. Here, this arrangement is studied at the presynaptic part of the neuromuscular junction (NMJ) in larval *Drosophila*. For the first time STED microscopy was applied to image parts of a whole organism rather than single cells or bacteria grown on a coverslip.

The synaptic communication is mediated by the fusion of neurotransmitter-filled vesicles with the presynaptic membrane at the active zone. This process is triggered by an influx of  $\text{Ca}^{2+}$  through clusters of voltage gated channels [57, 58]. For rapid communication, the synaptic vesicles must be held close to the calcium channels at the presynaptic membrane and precise positioning of the calcium channels is required [59].

In the *Drosophila* NMJ a protein named Bruchpilot (BRP) was found to have such an organizing role in forming the presynaptic density (so-called “T-bars”) [60]. At the NMJ of *Drosophila* mutants lacking this protein, the presynaptic densities are no longer present. Nevertheless, the nerve-evoked transmission still occurs but is reduced to around 25% of the normal function. BRP probably forms a matrix surrounding the calcium channels, but the form of the matrix has been unknown so far.

#### Imaging of the *Drosophila* neuromuscular junction

The monoclonal antibody Nc82 recognizes the Bruchpilot protein [60] and was used as the primary antibody for immunolabeling with Atto 532. The average power of the excitation and the STED beams at the sample were  $2.2 \mu\text{W}$  and 21 mW, respectively. The image was obtained by piezo-scanning of the sample at a pixel dwell time of 0.3 ms and a pixel spacing of  $20 \text{ nm} \times 20 \text{ nm}$  in the  $x$  and  $y$  direction. The raw image data were subjected to a single-step linear deconvolution with the respective PSF [61].

#### Results and discussion

With confocal microscopy, the Bruchpilot protein assemblies appear as broad spots at the active zones (Fig. 2.8 a). STED microscopy reveals that BRP forms flat, donut-shaped structures (Fig. 2.8 b). These ring-like structures can be seen more clearly after performing a linear deconvolution (Fig. 2.8 c). A comparison of the intensity profiles as obtained with confocal and STED

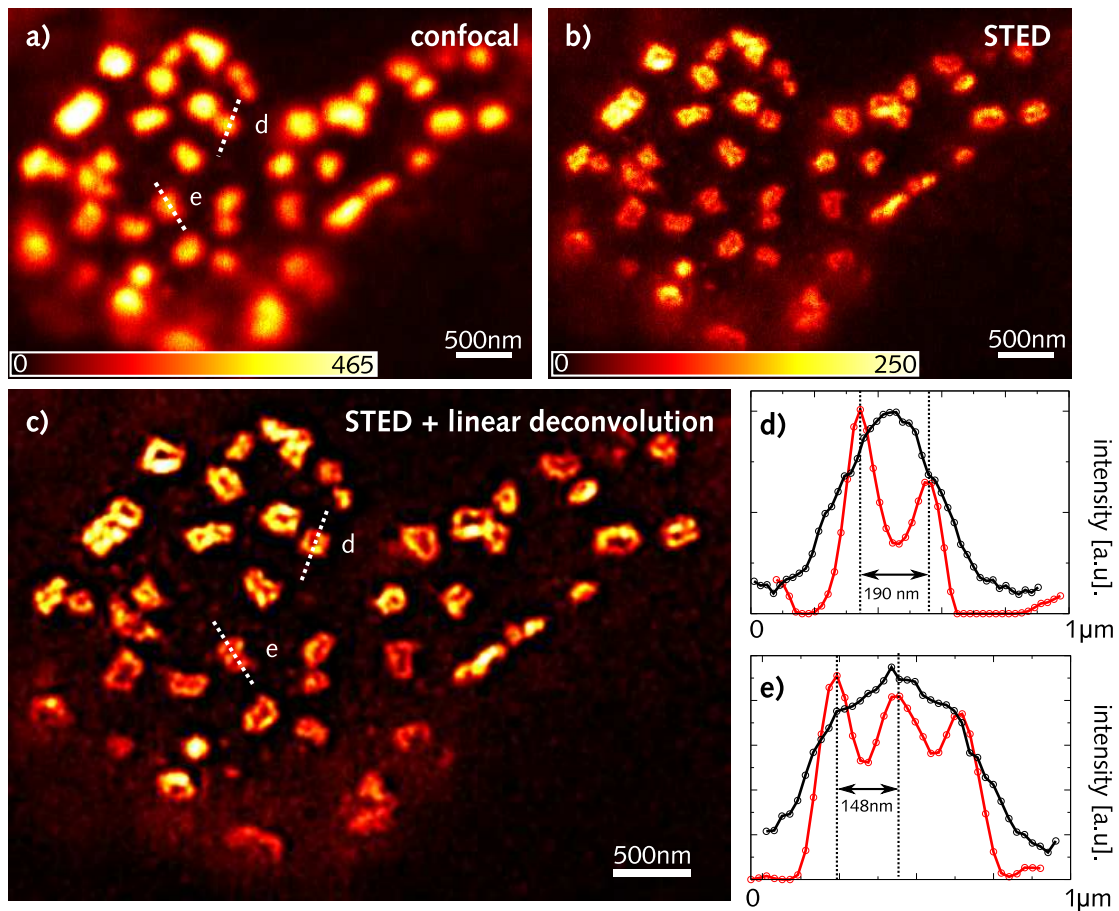


**Figure 2.8:** Confocal (a) and STED (b) images of the Bruchpilot protein in the *Drosophila* neuromuscular junction. The protein appears as large spots in the confocal image but ring-like structures become apparent in the STED image. This structure becomes even clearer after a linear deconvolution (c) with the effective PSF. The diameter of the rings in single and double ring structures was determined by measuring the distances between Gaussian fits to the respective intensity profiles of the boundaries. The graphs in d and e show the normalized intensity profiles of such structures as obtained with confocal (black) and STED (red) imaging.

imaging of these structures is given in Figs. (2.8 d) and (2.8 e). These structures consist of both single ring-like structures and multiple “rings”. The length of these rings could be measured by fitting a Gaussian distribution to the intensity profiles of the ring boundaries and determining the distance between their centers. The average length of isolated rings was  $190 \pm 2$  nm and rings inside double-ring structures showed an average length of  $148 \pm 2$  nm. When viewed perpendicular, these rings appeared to be flat, with a height up to 160 nm.

From transmission electron microscopy experiments and freeze-fracture images, there is some structural evidence that indicates that the active zone in the *Drosophila* NMJ normally consists of calcium channels and vesicles arranged along a T-bar [62, 63]. The appearance seen by STED

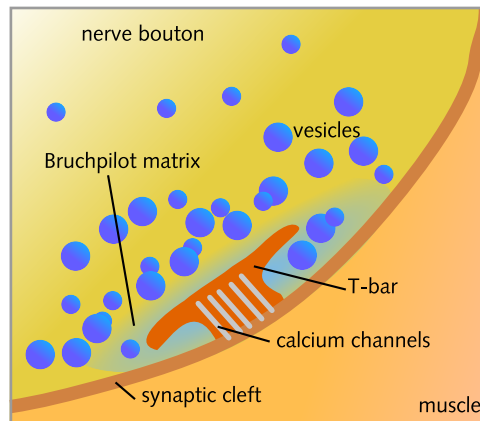


**Figure 2.9:** The schematic representation of the neuromuscular junction shows the role of the Bruchpilot protein: vesicles arriving at the presynaptic active zone (“T-bar”) trigger the release of  $\text{Ca}^{2+}$  into the synaptic cleft. The Bruchpilot matrix preserves the tightly packed structure of the calcium channels.

microscopy suggests that this aggregation of calcium channels is surrounded by a matrix of the Bruchpilot protein, which preserves the tight structure of the presynaptic active zone. This is necessary for the effectiveness of the presynaptic density, which acts as an attractor of synaptic vesicles and a guide to their optimal disposition [64].

## 2.5.2 STED microscopy for investigation of acetylcholine receptors

### Introduction

Rapid synaptic transmission as mediated by the neurotransmitter acetylcholine imposes requirements on concentration and spatial distribution of respective receptors to achieve high effectiveness. A characteristic feature of the postsynaptic membrane of innervated adult neuromuscular junctions is a high density of acetylcholine receptors (AChRs), tightly aggregated in the form of micron-sized two-dimensional clusters [65].

So far, epifluorescence and confocal microscopes fell short of resolving the fine structure of these small clusters. Therefore, STED microscopy was applied to visualize the organization of cell-surface AChRs supramolecular aggregates in the Chinese hamster ovary cell line CHO-K1/A5 below the diffraction resolution limit. In addition, cholesterol-dependent changes in the short and long range clustering behavior were investigated by size analysis and Ripley's K-test [66].

### Experimental procedures

**Sample preparation** A detailed description of the cell preparation is given in Appendix A.1. AChR in cells and in single plasma membrane sheets were investigated under different conditions. The membrane sheets were gained by disrupting the cells with a short ultrasound pulse. Cholesterol depletion was achieved by treating the cells with methyl- $\beta$ -cyclodextrin (CDx) (Sigma Chemical Co., USA).

In order to stain only cell-surface AChRs, CHO-K1/A5 cells were labeled with the monoclonal anti-AChR antibody mAb210 (Sigma Chemical Co.), followed by staining with secondary antibodies previously conjugated to the dye Atto 532. The latter was coupled to an affinity purified sheep anti-mouse IgG (Jackson ImmunoResearch Laboratories, USA) via its succinimidyl ester. For cholesterol dependent analysis, three different conditions were employed: In the "fix-label" condition, samples were fixed with 4% paraformaldehyde before labeling. Secondly, in the "label-fix" condition, fixation followed labeling to allow for antibody-induced AChR patching. Thirdly, when the effect of cholesterol depletion was studied ("CDx-label-fix"), samples were treated with CDx, stained with antibodies as described above and then fixed. The samples were mounted in Mowiol and imaged.

**Imaging of acetylcholine receptors** The average power of the excitation (490 nm) and the STED (615 nm) beams at the sample were  $2\ \mu\text{W}$  and  $14\ \text{mW}$ , respectively. The image was obtained by piezo-scanning of the sample at a pixel dwell time of 0.3 ms and a pixel spacing of  $15\ \text{nm} \times 15\ \text{nm}$  in the  $x$  and  $y$  directions.

**Data analysis** The FWHM of individual AChR nanoclusters was evaluated with macros written in Matlab (The Mathworks Inc., Natick, MA, USA) in  $7.5 \times 7.5\ \mu\text{m}^2$  images having a pixel spacing of  $15\ \text{nm} \times 15\ \text{nm}$ . The small dots resembled the Lorentzian intensity distribution of the effective STED PSF and the FWHM of the dots in the  $x$  and  $y$  direction were derived from Lorentzian fits. To ensure that the FWHM measurements were not affected by dots that were

close together, a stringent  $\chi^2$  cutoff of less than a 0.02 difference between the fit and the data was placed on the Lorentzian fit to the dots. The actual size of AChR nanoclusters was estimated by means of deconvolution with the effective point spread function in the STED mode.

For a quantitative analysis of the distribution of spatial point patterns, Ripley's K-test [66, 67] was incorporated. In particular, this method allows comparison of observed spatial point patterns with patterns of complete spatial randomness (CSR) on various length scales by taking into account the distance between all points in an area of interest. The expected number of neighbors  $N(r)$  for each individual particle within the distance  $r$  is characterized by Ripley's K-function:

$$N(r) = \rho K(r) \quad (2.9)$$

where  $\rho$  denotes the particle density of  $N$  individual particles in an area  $A$  ( $\rho = N/A$ ). In the case of CSR, the expected value of  $N(r)$  is  $\rho\pi r^2$  at any distance  $r$ , thus

$$K(r) = \pi r^2 \quad (\text{complete spatial randomness}) \quad (2.10)$$

$K(r)$  was calculated using an approximately unbiased estimator as suggested by Ripley [66, 67]:

$$K(r) = \frac{A}{N^2} \sum_{i=1}^N \sum_{j=1, j \neq i}^N w_{ij} k(i, j) \quad (2.11)$$

If the distance between the two particles  $i$  and  $j$  is smaller than  $r$ , then the counter variable  $k(i, j) = 1$ , otherwise it is zero. The weighting factor  $w_{ij}$  for border correction is  $1/(\text{fraction of the circumference of a circle centered in } i \text{ and passing through } j \text{ that lies within the analyzed area})$ , yielding in values between 1 and 4. Calculation of  $k(i, j)$  and  $w_{ij}$  from the particles' coordinates  $x$  and  $y$  follows from elementary trigonometry. For interpretation using the transformation

$$L(r) = \sqrt{K(r)/\pi} \quad (2.12)$$

and calculating  $L(r) - r$  is preferred, since  $L(r) - r = 0$  for random patterns.

The coordinates of the particles were extracted from the images by determining each particle's center of mass using custom-written software. The upper and lower value of the 99 % confidence interval (CI) were estimated by means of Monte Carlo simulations, where for each image the  $K(r)$  function for random patterns of same size and particle density was calculated. To allow averaging of data from different images, the estimated 99 % CI values were used to normalize each  $L(r)$  function for each image. Hence the 99 % CI will be shown as  $\pm 1$  lines in the resulting  $L(r) - r$  plots.

## Results

Imaging of cells and single plasma membrane sheets was performed in confocal and STED mode for two experimental conditions. First, fixation was followed by labeling ("fix-label"), thus avoiding long-range crosslinking of AChRs by the antibodies [68]. For the second condition ("label-fix"), the labeling procedure preceded fixation. This allowed crosslinkage between neighboring

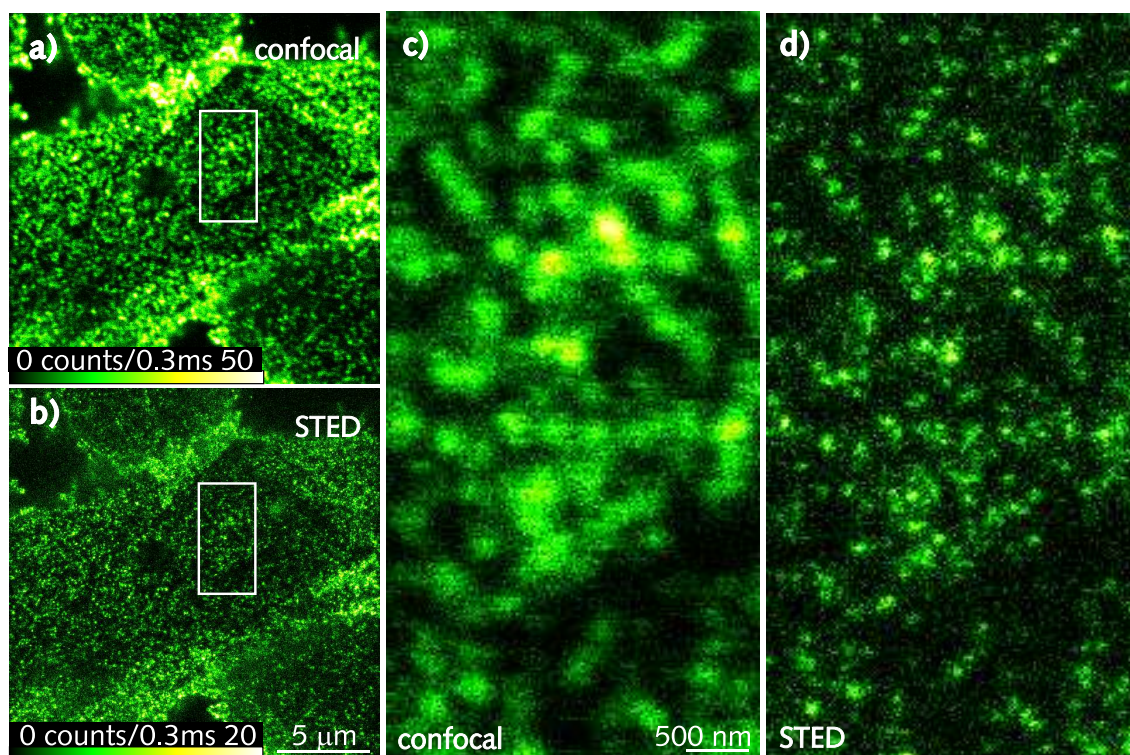


**Figure 2.10:** CHO-K1/A5 cells and membrane sheets on the same coverslip as imaged in confocal (a) and STED (b) mode. The high magnification areas (c and d) show that STED can resolve individual AChR nanoclusters.

AChRs. Using confocal microscopy, fluorescently labeled dots at the surface of the cells were revealed. The average FWHM of the measured spots was  $199 \pm 34$  nm and  $191 \pm 33$  nm when the specimens were “fix-label” and “label-fix”, respectively (see Figs. 2.10 and 2.11).

In STED imaging mode, the measured spots could be narrowed down to a FWHM of  $77 \pm 33$  nm and  $91 \pm 41$  nm for the two aforementioned experimental conditions, respectively. Side by side comparison of the confocal and the STED images in Fig. 2.10 makes the striking gain in resolution obvious. Because the measured spots represent a convolution of the particles with the finite effective PSF, the actual receptor agglomerations are in fact even smaller. Hence, when the antibody-induced clustering is inhibited by prior fixation, STED imaging resolves the blurred and uniformly distributed spots delivered by confocal microscopy into smaller AChR particles of variable size, with an estimated average diameter below 55 nm, hereafter referred to as AChR “nanoclusters”.

Comparing the conditions “fix-label” and “label-fix”, the small increase in the size distribution of AChR nanoclusters reflects the aggregation induced by the combined effect of primary (anti-AChR) and secondary (IgG) antibodies. Furthermore, a comparison of the size and intensity distribution of AChR nanoclusters in cells and spots in single membrane sheets revealed almost no difference for the two conditions tested. This finding indicates that the size distribution of

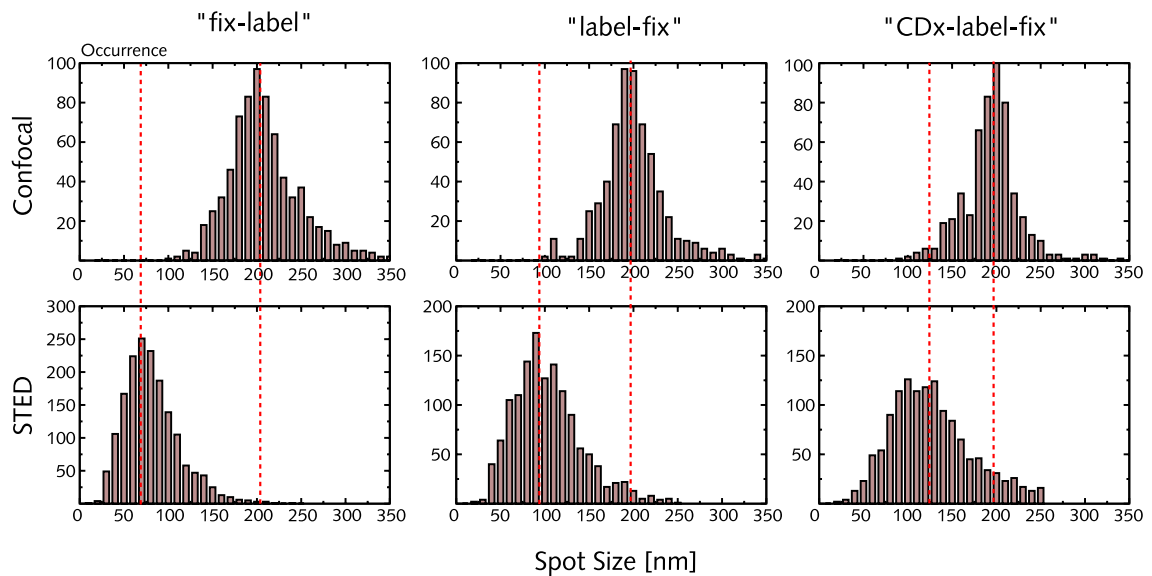


**Figure 2.11:** The size distribution of AChR nanoclusters as imaged in the confocal and the STED mode under three experimental conditions. The small AChR clusters can not be resolved with confocal microscopy and the size distribution is centered around 190 nm, corresponding to the confocal resolution limit. Due to this limited resolution, changes upon cholesterol depletion can not be seen, whereas a marked size increase upon cholesterol depletion is visible in STED microscopy. The total number of particles analyzed is indicated in Tab. 2.2.

AChR particles in membrane sheets and whole cells is essentially similar.

Cholesterol is one of the key lipid components involved in AChR functionality [69, 70]. Furthermore, cholesterol-enriched membrane domains have been postulated to concentrate signaling molecules and receptors in particular regions of the cell surface [71]. In order to investigate whether the organization of AChR particles at the cell surface was cholesterol-dependent a series of experiments was performed. To study the effect of cholesterol depletion from the cells these cells or membrane sheets were treated with CDx, stained with Atto 532 labeled antibodies and fixed (condition “CDx-label-fix”).

STED microscopy revealed changes in the distribution of AChR particles upon CDx treatment that were not detectable with confocal microscopy. The analysis of the size and fluorescence intensity distribution of AChR particles in the STED images exhibited a significant broadening of the size distribution upon cholesterol depletion (Fig. 2.11 and Tab. 2.2). This broadening stems from further aggregation of the small AChR particles, resulting in larger-sized AChR nanoclusters as detected by STED microscopy [72]. The distribution of AChR clusters in the STED images was also analyzed at larger scales by applying Ripley’s K-test for spatial randomness [66, 67]. As opposed to nearest neighbor methods, this second order analysis incorporates all inter-particle distances over the study area. The result is a thorough topographical characterization which in turn can be compared with that of a pattern resembling CSR. The data corresponding to whole cells in the “label-fix” condition imaged with STED microscopy showed a random distribution of

Condition	Mean spot size [nm]	Upper limit for estimated mean cluster size [nm]	Mean intensity [a.u.]
Whole cells			
“fix-label”	75.8 ± 32.4	53.8	347.7 ± 266.5 ( $n = 609$ )
“label-fix”	109.7 ± 35.7	95.3	955.5 ± 868.5 ( $n = 541$ )
“CDx-label-fix”	120.0 ± 44.7	110.1	797.3 ± 692.5 ( $n = 734$ )
Membrane Sheets			
“fix-label”	77.1 ± 32.9	55.1	323.4 ± 302.5 ( $n = 1075$ )
“label-fix”	91.3 ± 40.7	69.4	442.2 ± 409.4 ( $n = 817$ )
“CDx-label-fix”	131.1 ± 60.1	123.1	701.3 ± 874.4 ( $n = 616$ )

**Table 2.2:** Mean spot size and estimated cluster size distribution of AChR clusters under the three different conditions tested. The cluster size was estimated by means of convolution of simulated clusters with the measured effective point spread function. The figure in parentheses ( $n$ ) indicates the number of AChR particles analyzed in each case.

particles at all length scales, meaning the deviation from the  $L(r) - r = 0$  curve was within the 99 % CI expected for a random distribution. The same tendency is observed in plasma membrane sheets (see Fig. 2.12).

A change in the long-range organization of the AChR upon cholesterol depletion is observed. After cholesterol extraction from the cells, positive values of the  $L(r) - r$  function were observed within a narrow region of the  $r$  range analyzed; maximum deviation occurred at radii of 0.5–1  $\mu\text{m}$ , rapidly falling off to values below the cutoff limit for inter-cluster distances greater than 1.5  $\mu\text{m}$ . Thus, cholesterol depletion is accompanied by an increase in long-range interactions (as compared with the nanometer scale change in the AChR clusters themselves) and hence a change in AChR cluster distributions was made apparent by STED microscopy. The clustering of particles was clearly observed in intact cells, but was barely apparent in single membrane sheets, where it could be observed only for length scales between 0.6  $\mu\text{m}$  and 2  $\mu\text{m}$ .

**Discussion** Using STED microscopy it was possible to study changes in the size distribution of AChR nanoclusters well below the diffraction limit of a typical confocal microscope. The findings of the size distribution analysis indicate that the organization of AChR nanoclusters at the plasmalemma is indeed non-random, as well as cholesterol-dependent at scales below 250 nm. The results of the spatial point pattern analysis revealed that the long-range AChR organization at the plasmalemma of CHO-K1/A5 cells depends on cholesterol-sensitive interactions that normally extend over the range of a few microns in untreated cells. A likely candidate for the maintenance of such an influence is the cortical cytoskeleton and, particularly, the actin network.

The ability of AChR nanoclusters to aggregate upon cholesterol depletion in whole cells is apparently lost or substantially attenuated in single plasma membrane sheets devoid of the sub-cortical cytoskeleton. This provides additional, albeit indirect, evidence that the long-range AChR supramolecular organization is likely to be associated with the presence of an intact cytoskeletal

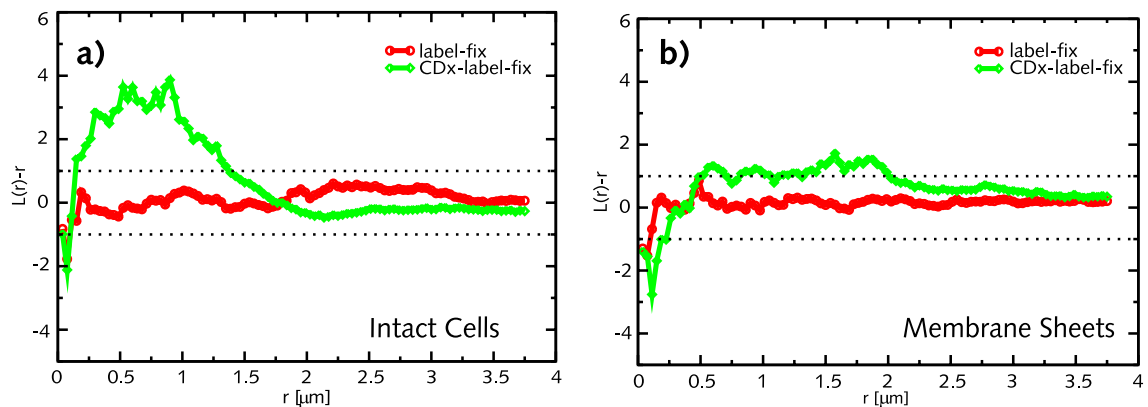


**Figure 2.12:** The statistical evaluation of the long-range AChR nanocluster organization makes apparent changes upon cholesterol depletion. Shown are plots of  $L(r) - r$  from Ripley's K-function analysis and their 99% CI intervals (dotted lines). The samples are randomly distributed in cells and membrane sheets before cholesterol extraction. Intact cells (a) show a stronger tendency to short-range ordering than membrane sheets (b) upon cholesterol depletion.

network under physiological energy supply and normal cholesterol levels. The short-range extent and composition of the AChR nanoclusters is probably maintained by protein-protein and receptor-lipid interactions, of which AChR-cholesterol interactions may constitute the prevailing stabilizing force [70].

## 3 STED microscopy with Q-switched microchip lasers

In the previous chapter it was shown that an illumination scheme utilizing a low repetition rate can result in a major signal increase in fluorescence microscopy and reduce photobleaching for dyes with the triplet as the predominant reactive state for photobleaching. Moreover, the shift from near infrared dyes to dyes emitting in the green to red range provided the ability to address biological questions with STED microscopy.

In this chapter it will be demonstrated how the STED microscope can be extended by utilizing Q-switched microchip lasers, exploiting their low repetition rate operation and their high energy pulses. Additionally, the range of dyes applicable to STED microscopy is further extended to dyes emitting in the blue range.

### 3.1 The shift to Q-switched microchip lasers and new dyes in the blue range

#### 3.1.1 A new approach with Q-switched microchip lasers

For the STED experiments carried out so far, very large, expensive and complex laser systems have been used. Due to the lack of stand-alone laser sources for efficient stimulated emission of dyes in the green to red range, nonlinear conversion systems, like an optical parametric oscillator, had to be used. In order to exploit the new illumination scheme at low repetition rates as described in section 2.4, the high repetition rate laser systems have to be altered in order to reduce the repetition rate. For example, a fast acousto-optic cell can be utilized to selectively discard unwanted pulses. Unfortunately, this also means that much power is lost in this way.

So far photobleaching of the dyes and a non-perfect zero intensity distribution in the PSF has restricted the applicable STED intensity. If photobleaching is substantially reduced and if a PSF with a high-quality local zero intensity can be provided, further increase of the STED intensity should lead to even higher resolution (see Eq. (1.5)). A possible laser system capable of delivering subpicosecond high-energy pulses at low repetition rates (250 kHz) and in the required wavelength range consists of the combination of a Ti:Sapphire laser, a regenerative amplifier (RegA) and an optical parametric amplifier (OPA). These well established systems are commercially available and can substitute the OPO systems. This approach was implemented and led to a further increase in resolution in another work [38].

	Ti:Sapphire/OPO	Ti:Sapphire/RegA/OPA	Q-switched microchip
repetition rate	80 MHz	250 kHz	10–100 kHz
pulse duration	< 100 fs	< 100 fs	1.5–2 ns
	$\approx 250$ ps (stretched)	$\approx 250$ ps (stretched)	
pulse energy	5 nJ	250 nJ	2 $\mu$ J
wavelength range	525–680 nm	480–700 nm	1064 nm, 532 nm

**Table 3.1:** A comparison of STED-relevant features between a Ti:Sapphire/OPO, Ti:Sapphire/RegA/OPA, and Q-switched microchip laser system.

From the screening experiments it was found that with depletion wavelengths below 550 nm competing two-photon excitation became a problem with the high power picosecond pulses delivered from an optical parametric oscillator. Therefore pulse durations in the nanosecond range are required to suppress unwanted multiphoton excitation by the STED beam. Since Ti:Sapphire/RegA/OPA systems are sensitive, expensive, difficult to handle and deliver subpicosecond pulses that can lead to unwanted two-photon excitation, other alternatives are of great interest.

One possibility to generate low repetition rate, high energy pulses are Q-switched microchip lasers. These lasers are usually compact, stable and easy-to-handle turn-key systems with nanosecond pulses. The relevant characteristics of such lasers and the previously utilized laser systems for STED-microscopy are illustrated in Tab. 3.1. The comparison shows that Q-switched microchip lasers are well suited for STED microscopy: The low repetition rate can readily be used to allow triplet relaxation. The pulse duration is on the one hand long enough to prevent nonlinear photo-damage effects or two-photon excitation; on the other hand it is still shorter than the fluorescence lifetime of the dyes commonly used in fluorescence microscopy, thus permitting sufficient stimulated emission. Also, the high energy pulses provide a very high photon flux favoring pronounced stimulated emission. The most prevalent Q-switched laser systems are the Nd:YAG emitting at 1064 nm and also commonly available as frequency doubled or tripled versions emitting at 532 nm and 355 nm.

### 3.1.2 Blue dyes for STED microscopy

The first STED experiments demonstrating an increase in resolution were carried out with dyes having an emission maximum between 680 nm and 700 nm [73]. Improvements in the STED technique and further experiments with these dyes delivered a very high axial resolution of 33 nm on dye monolayers and membrane-labeled bacteria [39]. A lateral effective PSF in one dimension of 16 nm on single fluorescent molecules was also achieved [74].

With the utilization of dyes emitting in the yellow-green range for STED microscopy, the first biological applications could be successfully addressed [41, 64] and the viability of the green and the yellow fluorescent protein for STED microscopy presented new possibilities to answer biological questions [75]. Accordingly, going to even shorter wavelengths and utilizing dyes emitting

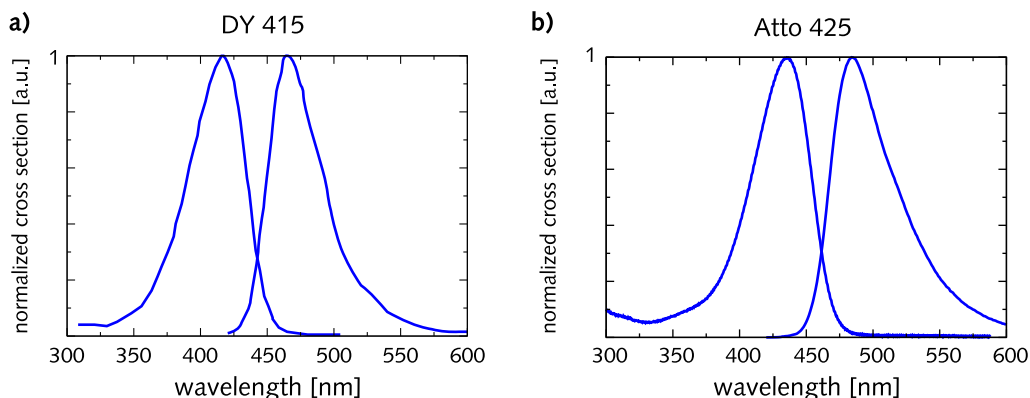


**Figure 3.1:** The excitation and emission spectra of the blue emitting dyes DY 415 (a) and Atto 425 (b) that were used for STED microscopy in the blue range.

in the blue range can extend the field of possible applications, and a shift to smaller wavelengths should lead to a further increase in resolution as predicted by Eq. (1.5). In addition, the possibility to utilize dyes in the whole visible spectrum for STED microscopy widens the field of applications.

In order to achieve an increased resolution with dyes emitting in the blue wavelength range with STED microscopy possible dyes and appropriate parameters for excitation and depletion had to be determined. The screening experiment described in section 2.3 already included blue emitting dyes, for example DAPI and several Coumarins. The blue emitting Coumarin-based dyes Atto 425 (Atto-Tec, Siegen, Germany) and DY 415 (Dyomics GmbH, Jena, Germany) turned out to be promising candidates for STED microscopy, because of their high quantum efficiency and photostability. Their absorption and emission spectra are shown in Fig. 3.1.

It was found that a low repetition rate illumination (for example 130 kHz) yielded an up to six-fold increase in the total fluorescence when compared to 40 MHz repetition rate illumination (data not shown). Moreover, adding the protective agents DABCO (1,4-diazabicyclo[2.2.2]octane, Sigma-Aldrich, Germany) or Cysteamine (Sigma-Aldrich, Germany) could further increase photostability and yielded an additional signal gain.

## 3.2 The STED setup using Q-switched microchip lasers

In order to explore the new possibilities by incorporating Q-switched microchip lasers and, on top of that, extending the range of dyes for STED microscopy further into the blue wavelength range, a new STED microscope was built. For this setup, a passively Q-switched microchip laser operating at  $\approx 65$  kHz repetition rate and a wavelength of 532 nm was used (Pulselas-P-532-60-CS, Alphalas GmbH, Göttingen, Germany). Due to the dramatic difference in repetition rate and pulse energy compared to the laser systems utilized in STED microscopy so far, several aspects of the setup needed to be reconsidered.

### 3.2.1 Pulse timing and beam shaping

Until now, usually modelocked lasers at 80 MHz and recently at 250 kHz repetition rate have been used for STED microscopy. These oscillators emit equidistant pulses with sub-picosecond jitter, which is very convenient for adjustment of the excitation and the STED pulse timing: The excitation diode can be triggered by any STED pulse and is then perfectly synchronized to the repetition rate of the master oscillator. An electronic delay pulse generator can then be used to achieve temporal overlap of the STED and the excitation pulse.

Q-switched lasers usually have a jitter of several microseconds, but a timing accuracy of the excitation and depletion pulses with picosecond precision is required. Therefore, the excitation pulse must coincide with exactly the STED pulse it was triggered by. The response time of the excitation diode (LDH-P-C-440B, Picoquant, Berlin, Germany) is around 50–100 ns, which means that the STED pulse, after having generated a trigger pulse, must pass an optical delay compensating for this response time. This can, for example, be achieved by utilizing optical fiber cables of appropriate length. However, the high pulse energy can cause substantial damage to the fiber end facet. In this setup, the light from the microchip laser was coupled into a 30 m long, polarization-maintaining single-mode fiber, corresponding to a delay of approximately 150 ns. To protect the fiber from damage, the input power was limited to 10 mW, corresponding to an average pulse energy of 150 nJ, with neutral density filters.

The timing of the detection also needs careful consideration: due to the high idle times of the system between successive pulses, only photons being detected within a certain time frame after an excitation pulse may contribute to the signal. This decreases the collection of background signal at times, where no signal due to the absence of excitation is expected. Therefore, the detection photon counting module used to record the signal (SPC-730, Becker & Hickl, Berlin, Germany) is time gated by the synchronization output of the excitation diode. This card operates in reverse start-stop mode and the time window for counting photons before a synchronization pulse arrives is 25.6 ns. Careful timing of the synchronization pulse and the counting signal via electronic cabling results in the suppression of background signal during idle times.

As outlined in section 2.2, several methods can be implemented to obtain the necessary PSF for STED microscopy. Spatial light modulators offer high flexibility and can be used over a wide range of wavelengths. However, they are not suited for the high peak intensities of Q-switched lasers. Binary phase masks are suitable for any power, but in order to obtain two-dimensional resolution improvement, the STED beam has to be split up into two parts and in the end, three laser beams need to be aligned with one another [76]. The recent availability of helical phase masks for a variety of wavelengths (VPP-A1, RPC Photonics, USA) offers the ability to create a donut-shaped focal spot with a high-quality zero. These polymer phase masks show almost no absorption of the laser light and are therefore suitable for high power applications. Accordingly, such a helical phase mask was incorporated into the setup for the creation of a donut shaped PSF.

### 3.2.2 Increasing the speed of Q-switched microchip laser STED microscopy

One of the advantages of Q-switched microchip lasers is their low repetition rate resulting in a signal gain in fluorescence microscopy. These lasers usually operate in the 10–50 kHz range, thus providing enough time for triplet relaxation, but also greatly reducing the recording speed. This is partly compensated for by the gain in total fluorescence and the fact that due to reduced photobleaching, higher excitation intensities can be applied [38]. Nevertheless, image acquisition time is a crucial factor for some applications. An increase of the repetition rate up to 500 kHz still suffices for suppressed photobleaching conditions and also allows faster imaging because of more excitation/fluorescence cycles per recording time interval. Although it was reported that passively Q-switched diode-pumped microchip lasers can be designed to have a repetition rate of up to 7 MHz [77], commercially available systems with nanosecond pulses seldomly exceed 50 kHz.

The laser utilized in this setup was already custom tuned to work at the repetition rate of 65 kHz with 1.5 ns pulses, and the following approach was chosen to achieve faster image acquisition: The laser beam is split into two beams that are recombined after introducing a path-difference between the beams. If such a path-difference spans several meters, a delay of several nanoseconds can be achieved. Thus the effective average repetition rate is artificially increased by a factor of two (see Fig. 3.2). In principle, this method can be employed multiple times but alignment becomes exceedingly difficult and also power losses might not permit further pulse-doubling.

In this setup, two polarizing beam-splitters (PBS) were used, because they provide beam splitting and recombination with very little losses. One of the beams is coupled into a 30 m long polarization-maintaining single-mode fiber before it is recombined with the original beam, thus separating the pulses by approximately 150 ns. Both spatially overlapped beams are then directed onto another fiber for spatially stable beam delivery into the microscope.

The effective repetition rate may be further increased by combining two lasers running at the

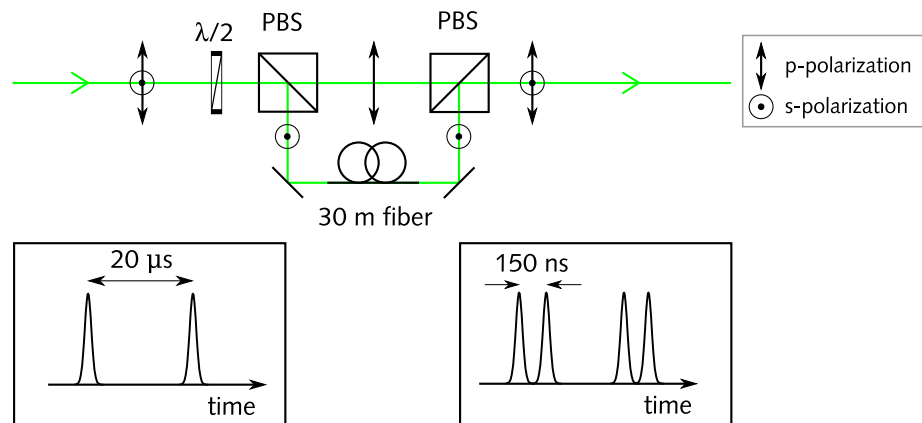


**Figure 3.2:** The image acquisition process is increased by splitting one pulse into two pulses with a delay of 150 ns. Polarizing beam-splitters (PBS) are utilized to reduce losses.

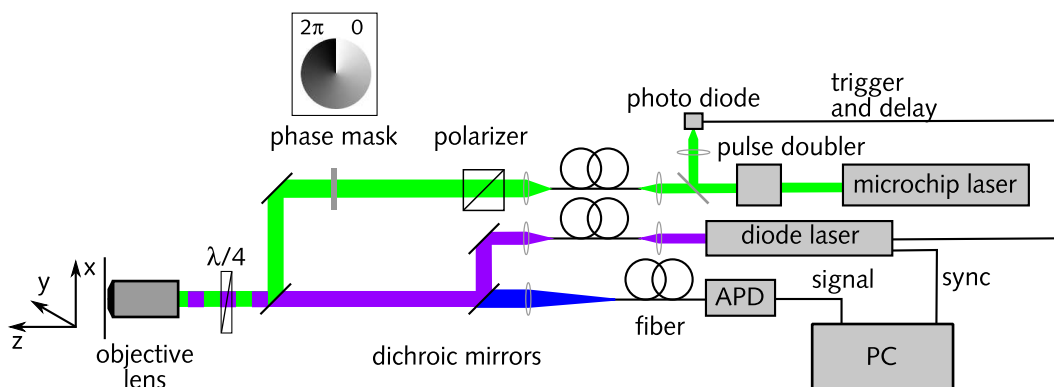


**Figure 3.3:** The STED setup with a Q-switched microchip laser for imaging in the blue wavelength range. The repetition rate is artificially doubled with the procedure described in section 3.2.2.

same repetition rate but with a spectral shift of a few nanometers. The two beams could then be combined by a dichroic mirror or by an acousto-optical filter. Afterwards, it is possible to double the pulses with the method described above, further increasing the effective average repetition rate.

Another possibility to accelerate the image acquisition process, besides increasing the repetition rate is to parallelize the scanning process, e. g. utilizing multiple foci which record several parts of the whole image simultaneously. In order to do so, new phase and amplitude patterns that create multiple donut-shaped STED foci were calculated in another work [78]. Although this concept is in principle possible, the SLMs that have been used so far are not capable of working with high intensity pulses as delivered by the Q-switched lasers. Furthermore alignment of several spots that can not necessarily be controlled individually imposes practical difficulties.

### 3.2.3 The final setup

The basic layout of the setup is shown in Fig. 3.3. The STED laser pulses are doubled, as described above, using two polarizing beam splitters. The beam then passes through a 4 % reflective glass plate which directs a portion of the light onto a fast photodiode to generate a trigger signal for the excitation diode. The beam is coupled into a 30 m long polarization-maintaining single-mode fiber for optical delay and spatially stable pulse delivery to the microscope. A polarizer ensures a well defined polarization state and the helical phase ramp is imprinted onto the beam with a polymer phaseplate (RPC Photonics, USA). The excitation diode (LDH-P-C-440B, Picoquant, Berlin, Germany) is externally triggered, emits pulses of less than 100 ps at 440 nm and is coupled into a polarization-maintaining single-mode fiber. Timing of the pulses is accomplished using a custom-built electronic delay.

The excitation and the depletion beam are both coupled into an oil immersion objective lens via appropriate dichroic mirrors (AHF Analysentechnik AG, Tübingen, Germany). Special objective lenses, optimized for blue and green wavelengths with a numerical aperture of 1.4 (UPlanSApo, 100×, Olympus, Olympus Co., Ltd., Tokyo, Japan) and 1.3 (ACS APO, 63×, Leica Microsys-

tems, Mannheim, Germany) were utilized in this setup. The fluorescence signal is collected via the objective lens, imaged onto a multimode fiber, and detected via an avalanche photodiode in the counting mode (SPCM-AQR-13-FC, PerkinElmer OptoElectronics Europe, Germany). The core diameter of the fiber and the focal length of the tube lens were chosen to provide a detection pinhole diameter corresponding to 70–80% of the extent of the backprojected Airy disk. Image formation is accomplished by piezo-stage scanning of the sample (Nanoblock, Melles Griot, Cambridge, UK). The counting signals from the avalanche photodiode are recorded by a single-photon counting module (SPC-730, Becker & Hickl GmbH, Berlin, Germany) and time-gated by the synchronization output of the excitation diode driver.

### 3.3 Sub-diffraction resolution demonstrated

Several experiments with the above described setup were carried out in order to demonstrate the feasibility of Q-switched microchip lasers for STED microscopy with diffraction-unlimited resolution.

#### Imaging fluorescent nanoparticles

In order to determine the imaging capability of the microscope, fluorescent nanoparticles (beads) with a mean diameter of approximately 25 nm were imaged. The beads were produced following the protocol described in Appendix A.2.3 and stained with Atto 425. For imaging, the beads were sonicated for at least 10 minutes and adhered to Poly-L-lysine (Sigma-Aldrich, Germany) treated glass coverslips. The coverslips with a homogeneous distribution of nanoparticles was mounted with a 20 mM solution of DABCO (Sigma-Aldrich, Germany) onto a microscope slide for imaging.

The average excitation and STED power at the sample were 25 nW and 30  $\mu$ W at 125 kHz repetition rate, respectively. Several images using the 1.4 NA objective lens were recorded with a pixel spacing of 15 nm  $\times$  15 nm, both in the confocal and the STED mode, by turning the STED beam on and off for the according measurement (see Fig. 3.4). In the confocal image the small beads appear blurred and close particles could not be resolved. The STED image makes the gain in resolution apparent, where nearby particles can be resolved and the spots are much smaller.

The size of the fluorescent spots was determined by fitting Gaussian (confocal) and Lorentzian (STED) distributions to the intensity profiles of the beads with custom Matlab routines. The FWHMs were extracted from the fits, yielding  $163.9 \pm 6.6$  nm in the confocal and  $54.0 \pm 3.4$  nm in the STED imaging mode. These spots represent a convolution of the effective PSF with the beads object function and represent merely an upper limit for the resolution capability of the microscope. It can be calculated that the actual FWHM of the STED PSF, and hence the resolution of the microscope is below 25 nm. In comparison with the resolution limit given by Abbe,  $\lambda/2NA = 157$  nm, this corresponds to a more than 6 fold gain in focal plane resolution and an approximately 40 fold reduction of the lateral focal spot area.

This is the first demonstration of STED microscopy with a resolution below 25 nm utilizing Q-switched microchip lasers and blue emitting dyes.

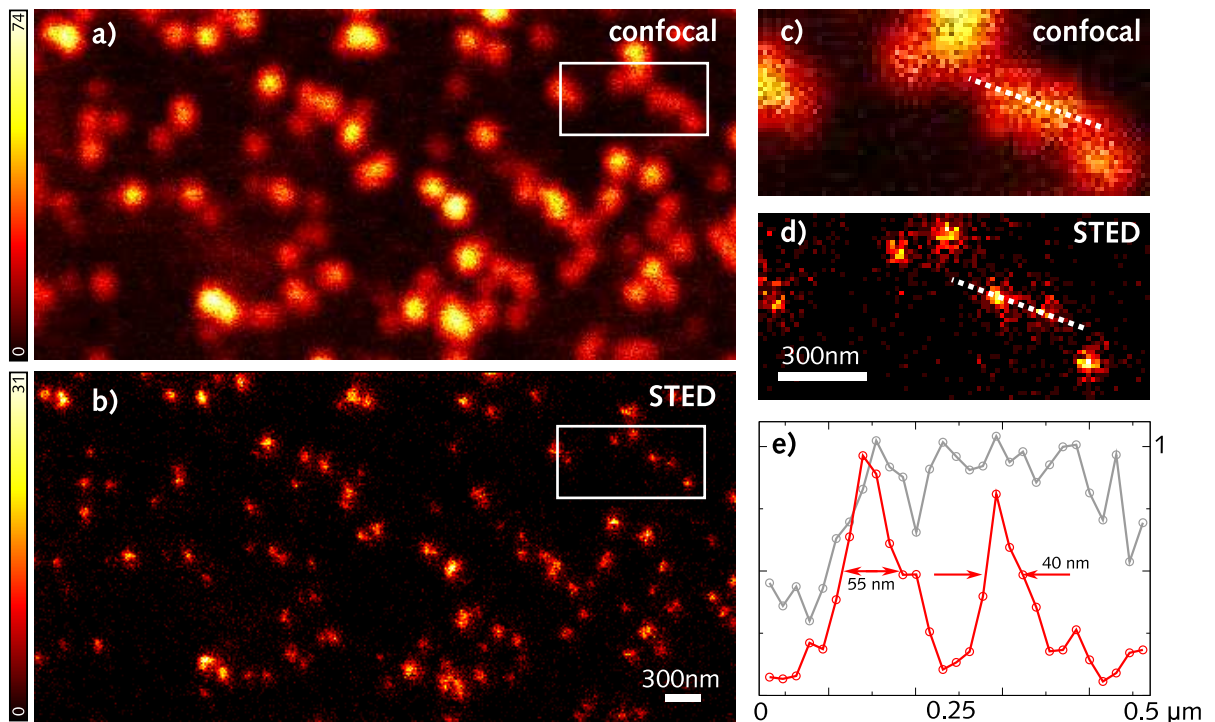


**Figure 3.4:** Fluorescent nanoparticles of 25 nm diameter as imaged with confocal (a) and STED (b) microscopy. The high magnification areas c and d illustrate the high resolution of the STED microscope. The normalized intensity profiles (e) show a FWHM as low as 40 nm in the STED image.

### Improved resolution in biological samples

One of the main applications of STED microscopy is the investigation of biological samples. Here, the resolution improvement using a Q-switched microchip laser and dyes emitting in the blue range is demonstrated by imaging nanometer sized clathrin protein assemblies below the diffraction limit.

**Introduction** Cells communicate and exchange material by means of numerous membrane-enclosed transport packages. These packages can be small spherical vesicles or larger, irregular vesicles or membrane fragments. Vesicles carrying soluble molecules or membrane components, referred to as cargo, continually form and separate from one membrane and fuse with another membrane. This traffic within or between cells is highly organized, and in order to perform its function each transport vesicle must take up only the appropriate cargo and fuse with the appropriate target membrane.

Most transport vesicles bud off as coated vesicles. The coat serves two principal functions: First, it helps to concentrate specific membrane proteins in a certain area of the membrane and second, the coat proteins assemble in curved, basket-like lattices, thus deforming the membrane and molding the forming vesicles. There are several types of coat proteins, one of which is the

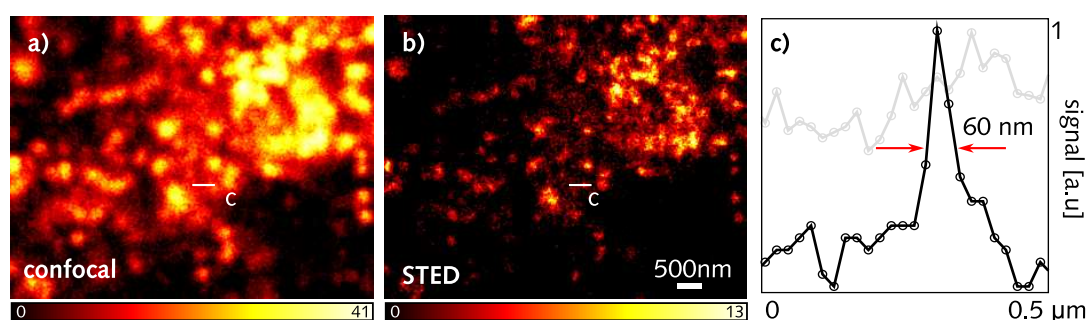


**Figure 3.5:** The same region showing clathrin imaged in the confocal (a) and STED (b) mode. With STED microscopy finer details can be resolved and the intensity profiles of individual clathrins show a FWHM as low as 60 nm (c).

clathrin protein [79].

The clathrin protein shows a three legged structure called a triskelon, which assembles into a basketlike convex framework of hexagons and pentagons to form the coat around the vesicles. Whole clathrin baskets forming without a vesicle can be between 48 nm and 55 nm [80] and the smallest intact coated vesicles are about 75 nm in diameter but can be as large as 300 nm [80]. Due to the small diameters, the clathrin assemblies serve as interesting objects for STED microscopy. However, the size of the clathrin baskets is still too large to demonstrate the full resolution capability of the microscope.

**Experimental procedures and imaging** Cells from the mammalian epithelial cell line PtK2 (*Potorous tridactylus*) were fixed in 3.7 % paraformaldehyde and anti-clathrin heavy chain rabbit IgG (Biozol GmbH, Eching, Germany) was used as the primary antibody. The dye DY 415 (Dyomics GmbH, Jena, Germany) was conjugated to sheep anti-rabbit IgG (Dianova GmbH, Hamburg, Germany) via its succinimidyl ester and used for labeling of the clathrin protein.

Imaging was performed using the above described setup with a  $63\times$  oil immersion objective lens of 1.3 NA. The average excitation and STED power at the sample was 50 nW and  $200\ \mu\text{W}$  at 130 kHz, respectively. The images with a pixel spacing of  $20\ \text{nm} \times 20\ \text{nm}$  were recorded simultaneously in the confocal and the STED mode by turning the STED beam on and off.

**Results and discussion** The images obtained in standard confocal microscopy show broad fluorescent spots and clusters of fluorescently labeled clathrin. A gain in resolution becomes apparent when the same region is imaged with STED microscopy (see Fig. 3.5). The FWHM of several clathrin assemblies was determined by fitting a Gaussian (confocal) and Lorentzian (STED) distribution to the respective intensity profiles. The average FWHM of the spots for the confocal case was  $235.5 \pm 4.1\ \text{nm}$ . With STED an average FWHM of  $104.7 \pm 6.6\ \text{nm}$  was determined, but spots with a FWHM as low as 60 nm were also found.

The results show that using STED microscopy with Q-switched microchip lasers and blue emitting dyes can be applied to biological samples with much higher resolution than that attainable with confocal microscopy.

## 4 Conclusion and outlook

In this thesis several methods and concepts to develop the STED microscope further have been illustrated. The examination of the fluorescence and bleaching behavior under different illumination repetition rates revealed a substantial signal increase and reduced photobleaching for repetition rates below several kilohertz. This is achieved by providing enough time for molecules which are caught in the nonfluorescent triplet state to relax back to the ground state. The average emitted fluorescence of the dye is increased and at the same time photobleaching from the triplet state is diminished. Furthermore it could be exemplified how STED-induced photobleaching from the singlet and the triplet state can be distinguished by determining the relationship between photobleaching and the delay between excitation and STED pulses.

The STED technique using dyes emitting in the visible range was further established as a valuable tool in cell biology. The high lateral resolution beyond the diffraction barrier revealed that the Bruchpilot protein at the presynaptic active zone of larval *Drosophila* neuromuscular junctions forms flat, ring-like structures of diameters around 190 nm for isolated rings and 148 nm in double rings [64]. These structures were not resolvable with standard confocal microscopy. From the STED images together with transmission electron microscopy images, it was found that the Bruchpilot protein forms a matrix around presynaptic active densities, so called “T-bars”, enabling a tight cluster formation of  $\text{Ca}^{2+}$  channels necessary for rapid synaptic communication.

In another application, the cholesterol dependent clustering of the nicotinic acetylcholine receptor (AChR) was studied. The sub-diffraction resolution of the STED microscope enabled the observation of an increase in the average AChR cluster size from less than 55 nm up to 125 nm upon cholesterol depletion of the plasma membrane [72]. These cluster sizes are well below the diffraction limit of far-field light microscopes and are not observable in this manner with standard fluorescence microscopy. Furthermore the long-range organization and its cholesterol dependence was investigated by means of statistical analysis, revealing the development of short-range organization upon cholesterol depletion. This development is more pronounced in intact cells than in membrane sheets and the organization of nanoclusters is therefore likely associated with the presence of an intact cytoskeletal network [72].

In this thesis, for the first time a successful shift from complex, high-repetition rate laser systems to the more compact, low repetition rate, easy-to-use and low cost Q-switched microchip lasers for STED microscopy was demonstrated. From imaging colloidal nanoparticles with a mean diameter of 25 nm it was concluded that the FWHM of the STED microscopes effective PSF is less than 25 nm. Imaging of biological structures beyond the diffraction limit was successfully demonstrated with clathrin proteins.

Nevertheless, the great potential of Q-switched lasers for STED microscopy has not yet been fully exploited. For example, nonlinear effects in standard optical fibers or microstructured photonic crystal fibers (PCFs) may be exploited for supercontinuum generation [81]. From experiments performed during this work, it was found that the coupling efficiency for PCFs is usually not better than 60 % and the intensity is spread over a wide wavelength range, thus rendering Ti:Sapphire-based supercontinuum generation unsuitable for STED microscopy (data not shown). The very high pulse energy of Q-switched lasers however, may provide enough intensity in the PCF's output spectrum for sufficient stimulated emission depletion. Hence, one Q-switched laser can possibly be used for multicolor STED microscopy in the whole visible range with unsurpassed resolution.

The high intensity provided by Q-switched lasers may also be employed to generate two separate STED beams, one for an increase in the lateral, the other for an increase in the axial direction, thus realizing a STED microscope with diffraction-unlimited 3D resolution. Hence, this thesis forms the basis for further improvements in the STED technique, that are likely to be realized in the near future.

The successful application to cell biology is among other things a result of the shift to dyes emitting in the visible, namely the green to red range for STED microscopy. At the same time, this development opened the possibility for two-color STED microscopy [82]. This thesis extends the spectrum of suitable dyes for STED microscopy into the blue range, thus widening the field of possible applications even further.

# Bibliography

- [1] R. Hooke. *Micrographia*. Octavo, London, first edition, 1665.
- [2] E. Abbe. Beiträge zur Theorie des Mikroskops und der mikroskopischen Wahrnehmung. *Archiv für Mikroskopische Anatomie*, 9:413–420, 1873.
- [3] M. Knoll and E. Ruska. Beitrag zur geometrischen Elektronenoptik I. *Annalen der Physik*, 12(5):607–640, 1932.
- [4] M. Knoll and E. Ruska. Beitrag zur geometrischen Elektronenoptik II. *Annalen der Physik*, 12(6):641–661, 1932.
- [5] M. Knoll and E. Ruska. Das Elektronenmikroskop. *Zeitschrift für Physik*, 78:318–339, 1932.
- [6] A. I. Kirkland and L. Hutchinsons. Atomic resolution transmission electron microscopy. In P. W. Hawkes and J. C. H. Spence, editors, *Science of Microscopy*, volume I, chapter 1, pages 3–64. Springer, 2007.
- [7] F. de Lange, A. Cambi, R. Huijbens, B. de Bakker, W. Rensen, M. Garcia-Parajo, N. van Hulst, and C. G. Figdor. Cell biology beyond the diffraction limit: near-field scanning optical microscopy. *Journal of Cell Science*, 114(23):4153–4160, 2001.
- [8] H. Siedentopf and R. Zsigmondy. Visualisation and determination of size of ultra microscopic particles, with special use of Goldrubin glasses. *Annalen der Physik*, 10(1):1 – 39, 1902.
- [9] F. Zernike. Inflection theory of the cutting method and its improved form, the phase contrast method. *Physica*, 1:689–704, 1934.
- [10] F. Zernike. The phase contrast process in microscopic examinations. *Physikalische Zeitschrift*, 36:848–851, 1935.
- [11] P. I. Bastiaens and A. Squire. Fluorescence lifetime imaging microscopy: spatial resolution of biochemical processes in the cell. *Trends in Cell Biology*, 9(2):48–52, 1999.
- [12] B. Valeur. *Molecular Fluorescence*. Wiley-VCH, Weinheim, 2002.
- [13] E. A. Jares-Erijman and T. M. Jovin. FRET imaging. *Nature Biotechnology*, 21(11):1387–1395, 2003.

- [14] T. K. L. Meyvis, S. C. De Smedt, P. Van Oostveldt, and J. Demeester. Fluorescence recovery after photobleaching: A versatile tool for mobility and interaction measurements in pharmaceutical research. *Pharmaceutical Research*, 16(8):1153–1162, 1999.
- [15] E. A. J. Reits and J. J. Neefjes. From fixed to FRAP: Measuring protein mobility and activity in living cells. *Nature Cell Biology*, 3:E145–E147, 2001.
- [16] J. Lippincott-Schwartz and G. H. Patterson. Development and use of fluorescent protein markers in living cells, 2003.
- [17] M. Minsky. Microscopy apparatus, 1961. US Patent 3,013,467.
- [18] S. Inoue. Foundations of confocal scanned imaging in light microscopy. *Handbook of Biological Confocal Microscopy*, pages 1–18, 1995.
- [19] W. Denk, J. H. Strickler, and W. W. Webb. Two-photon laser scanning fluorescence microscopy. *Science*, 248:73–76, 1990.
- [20] F. Helmchen and W. Denk. Deep tissue two-photon microscopy. *Nature Methods*, 2(12):932–940, 2005.
- [21] W. R. Zipfel, R. M. Williams, and W. W. Webb. Nonlinear magic: multiphoton microscopy in the biosciences. *Nature Biotechnology*, 21(11):1369–1377, 2003.
- [22] M. Born and E. Wolf. *Principles of Optics*. Pergamon Press, Oxford, 6th edition, 1993.
- [23] K. König. Multiphoton microscopy in life sciences. *Journal of Microscopy*, 2000.
- [24] S. Hell and E. H. K. Stelzer. Properties of a 4Pi confocal fluorescence microscope. *Journal of the Optical Society of America A*, 9(12):2159–2166, 1992.
- [25] A. Egner, S. Jakobs, and S. W. Hell. Fast 100-nm resolution three-dimensional microscope reveals structural plasticity of mitochondria in live yeast. *Proceedings of the National Academy of Sciences*, 99(6):3370–3375, 2002.
- [26] J. Pawley. *Handbook of biological confocal microscopy*. Plenum Press, New York, 1995.
- [27] E. B. Shera, N. K. Seitzinger, L. M. Davis, R. A. Keller, and S. A. Soper. Detection of single fluorescent molecules. *Chemical Physics Letters*, 174(6):553–557, 1990.
- [28] A. Yildiz, J. N. Forkey, S. A. McKinney, T. Ha, Y. E. Goldman, and P. R. Selvin. Myosin V walks hand-over-hand: Single fluorophore imaging with 1.5-nm localization. *Science*, 300(5628):2061–2065, 2003.
- [29] E. Betzig, G. H. Patterson, R. Sougrat, O. W. Lindwasser, S. Olenych, J. S. Bonifacino, M. W. Davidson, J. Lippincott-Schwartz, and H. F. Hess. Imaging intracellular fluorescent proteins at nanometer resolution. *Science*, 313(5793):1642–1645, 2006.

- [30] M. J. Rust, M. Bates, and X. W. Zhuang. Sub-diffraction-limit imaging by stochastic optical reconstruction microscopy (STORM). *Nature Methods*, 3(10):793–795, 2006.
- [31] A. Sharonov and R. M. Hochstrasser. Wide-field subdiffraction imaging by accumulated binding of diffusing probes. *Proceedings of the National Academy of Sciences of the United States of America*, 103(50):18911–18916, 2006.
- [32] S. W. Hell, M. Dyba, and S. Jakobs. Concepts for nanoscale resolution in fluorescence microscopy. *Current Opinion in Neurobiology*, 14(5):599–609, 2004.
- [33] S. W. Hell and J. Wichmann. Breaking the diffraction resolution limit by stimulated emission: stimulated-emission-depletion fluorescence microscopy. *Optics Letters*, 19(11):780–782, 1994.
- [34] S. W. Hell and M. Kroug. Ground-state-depletion fluorescence microscopy: A concept for breaking the diffraction resolution limit. *Applied Physics B: Lasers and Optics*, 60(5):495–497, 1995.
- [35] M. Hofmann, C. Eggeling, S. Jakobs, and S. W. Hell. Breaking the diffraction barrier in fluorescence microscopy at low light intensities by using reversibly photoswitchable proteins. *Proceedings of the National Academy of Sciences*, 102(49):17565–17569, 2005.
- [36] H. Haken and H. C. Wolf. *Molekülphysik und Quantenchemie*. Springer, 1992.
- [37] S. W. Hell and A. Schönle. Nanoscale resolution in far-field fluorescence microscopy. In P. W. Hawkes and J. C. H. Spence, editors, *Science of Microscopy*, volume II, pages 790–834. Springer, 2007.
- [38] G. Donnert, J. Keller, R. Medda, M. A. Andrei, S. O. Rizzoli, R. Luhrmann, R. Jahn, C. Eggeling, and S. W. Hell. Macromolecular-scale resolution in biological fluorescence microscopy. *Proceedings of the National Academy of Sciences*, 103(31):11440, 2006.
- [39] M. Dyba and S. W. Hell. Focal spots of size  $\lambda/23$  open up far-field fluorescence microscopy at 33 nm axial resolution. *Physical Review Letters*, 88(16):163901, 2002.
- [40] J. J. Sieber, K. I. Willig, R. Heintzmann, S. W. Hell, and T. Lang. The SNARE motif is essential for the formation of syntaxin clusters in the plasma membrane. *Biophysical Journal*, 90(8):2843–2851, 2006.
- [41] K. I. Willig, S. O. Rizzoli, V. Westphal, R. Jahn, and S. W. Hell. Sted-microscopy reveals that synaptotagmin remains clustered after synaptic vesicle exocytosis. *Nature*, 440(7086):935–939, 2006.
- [42] M. Dyba and S. W. Hell. Photostability of a fluorescent marker under pulsed excited-state depletion through stimulated emission. *Applied Optics*, 42(25):5123–5129, 2003.

- [43] J. Keller, A. Schönle, and S. W. Hell. Efficient fluorescence inhibition patterns for RESOLFT microscopy. *Optics Express*, 15(6):3361–3371, 2007.
- [44] Y. Igasaki, F. Li, N. Yoshida, H. Toyoda, T. Inoue, N. Mukohzaka, Y. Kobayashi, and T. Hara. High efficiency electrically-addressable phase-only spatial light modulator. *Optical Review*, 6(4):339–344, 1999.
- [45] M. Schwertner, M. Booth, and T. Wilson. Characterizing specimen induced aberrations for high NA adaptive optical microscopy. *Optics Express*, 12(26):6540–6552, 2004.
- [46] E. Rittweger, B. Rankin, V. Wesphal, and S. W. Hell. Fluorescence depletion mechanisms in super-resolving sted microscopy. *submitted*.
- [47] C. Eggeling, J. Widengren, R. Rigler, and C. A. M. Seidel. Photostability of Fluorescent Dyes for Single-Molecule Spectroscopy. *Applied Fluorescence in Chemistry, Biology and Medicine*, 1999.
- [48] P. S. Dittrich and P. Schwill. Photobleaching and stabilization of fluorophores used for single-molecule analysis. with one-and two-photon excitation. *Applied Physics B: Lasers and Optics*, 73(8):829–837, 2001.
- [49] S. Reindl and A. Penzkofer. Higher excited-state triplet-singlet intersystem crossing of some organic dyes. *Chemical Physics*, 211(1):431–439, 1996.
- [50] L. A. Deschenes and V. B. DA. Single molecule photobleaching: increasing photon yield and survival time through suppression of two-step photolysis. *Chemical Physics Letters*, 365(5):387–395, 2002.
- [51] T. G. Pavlopoulos and D. J. Golich. Triplet extinction coefficients of some laser dyes I. *Journal of Applied Physics*, 64(2):521–527, 1988.
- [52] James B. Pawley (ed.). *Handbook of biological confocal microscopy*. Springer, New York, 3rd edition, 2006.
- [53] G. Donnert, C. Eggeling, and S. W. Hell. Major signal increase in fluorescence microscopy through dark-state relaxation. *Nature Methods*, 4(1):81–86, 2007.
- [54] A. Charpilienne, M. Nejmeddine, M. Berois, N. Perez, E. Neumann, E. Hewat, G. Trugnan, and J. Cohen. Individual rotavirus-like particles containing 120 molecules of fluorescent protein are visible in living cells. *Journal of Biological Chemistry*, 276(31):29361–29367, 2001.
- [55] R. Y. Tsien and A. Waggoner. Fluorophores for confocal microscopy: photophysics and photochemistry. *Handbook of Biological Confocal Microscopy*, pages 153–161, 1990.

- [56] J. Widengren, A. Chmyrov, C. Eggeling, P. A. Löfdal, and C. A. M. Seidel. Strategies to improve photostabilities in ultrasensitive fluorescence spectroscopy. *Journal of Physical Chemistry A*, 111(3):429–440, 2007.
- [57] B. Katz and R. Miledi. The effect of calcium on acetylcholine release from motor nerve terminals. *Proceedings of the Royal Society of London. Series B, Biological Sciences*, 161(985):496–503, 1965.
- [58] R. G. Zhai and H. J. Bellen. The architecture of the active zone in the presynaptic nerve terminal. *Physiology*, 19(5):262–270, 2004.
- [59] E. F. Stanley. The calcium channel and the organization of the presynaptic transmitter release face. *Trends in Neurosciences*, 20(9):404–9, 1997.
- [60] D. A. Wagh, T. M. Rasse, E. Asan, A. Hofbauer, I. Schwenkert, H. Dürrbeck, S. Buchner, M. C. Dabauvalle, M. Schmidt, and G. Qin. Bruchpilot, a protein with homology to ELKS/CAST, is required for structural integrity and function of synaptic active zones in *Drosophila*. *Neuron*, 49(6):833–844, 2006.
- [61] A. N. Tikhonov, V. I. A. Arsenin, et al. *Solutions of Ill-posed Problems*. Wiley New York, 1977.
- [62] A. Prokop and I. A. Meinertzhagen. Development and structure of synaptic contacts in *Drosophila*. *Seminars in Cell & Developmental Biology*, 2005.
- [63] C. J. Feeney, S. Karunanithi, J. Pearce, C. K. Govind, and H. L. Atwood. Motor nerve terminals on abdominal muscles in larval flesh flies, *sarcophaga bullata*: Comparisons with *Drosophila*. *The Journal of Comparative Neurology*, 402(2):197–209, 1998.
- [64] R. J. Kittel, C. Wichmann, T. M. Rasse, W. Fouquet, M. Schmidt, A. Schmid, D. A. Wagh, C. Pawlu, R. R. Kellner, K. I. Willig, and others others. Bruchpilot promotes active zone assembly, Ca<sup>2+</sup> channel clustering, and vesicle release, 2006.
- [65] J. R. Sanes and J. W. Lichtman. Induction, assembly, maturation and maintenance of a postsynaptic apparatus. *Nature Review Neuroscience*, 2(11):791–805, 2001.
- [66] B. D. Ripley. Modelling spatial patterns. *Journal of the Royal Statistical Society, Series B*, 39(2):172–212, 1977.
- [67] B. D. Ripley. Tests of randomness for spatial point patterns. *Journal of the Royal Statistical Society. Series B (Methodological)*, 41(3):368–374, 1979.
- [68] S. Tzartos, S. Hochschwender, P. Vasquez, and J. Lindstrom. Passive transfer of experimental autoimmune myasthenia gravis by monoclonal antibodies to the main immunogenic region of the acetylcholine receptor. *Journal of Neuroimmunology*, 15(2):185–94, 1987.

- [69] F. J. Barrantes. Transmembrane modulation of nicotinic acetylcholine receptor function. *Current Opinion in Drug Discovery & Development*, 6:620–632, 2003.
- [70] F. J. Barrantes. Structural basis for lipid modulation of nicotinic acetylcholine receptor function. *Brain Research Reviews*, 47(1-3):71–95, 2004.
- [71] F. R. Maxfield. Plasma membrane microdomains. *Current Opinion in Cell Biology*, 14:483–487, 2002.
- [72] R. R. Kellner, C. J. Baier, K. I. Willig, S. W. Hell, and F. J. Barrantes. Nanoscale organization of nicotinic acetylcholine receptors revealed by stimulated emission depletion microscopy. *Neuroscience*, 2006.
- [73] T. A. Klar and S. W. Hell. Subdiffraction resolution in far-field fluorescence microscopy. *Optics Letters*, 24(14):954–956, 1999.
- [74] V. Westphal and S. W. Hell. Nanoscale resolution in the focal plane of an optical microscope. *Physical Review Letters*, 94:143903, 2005.
- [75] K. I. Willig, R. R. Kellner, R. Medda, B. Hein, S. Jakobs, and S. W. Hell. Nanoscale resolution in GFP-based microscopy. *Nature Methods*, 3:721–723, 2006.
- [76] T. A. Klar, E. Engel, and S. W. Hell. Breaking abbe’s diffraction resolution limit in fluorescence microscopy with stimulated emission depletion beams of various shapes. *Physical Review E*, 64:066613, 1–9, 2001.
- [77] B. Braun, F. X. Kartner, G. Zhang, M. Moser, and U. Keller. 56-ps passively Q-switched diode-pumped microchip laser. *Optics Letters*, 22(6):381–383, 1997.
- [78] J. Keller. *Optimal de-excitation patterns for RESOLFT-microscopy*. PhD thesis, Rupertus Carola University of Heidelberg, 2006.
- [79] B. Alberts, A. Johnson, J. Lewis, M. Raff, K. Roberts, and P. Walter. *Molecular biology of the cell*. Garland Science, New York, 4 edition, 2002.
- [80] J. Heuser. Three-dimensional visualization of coated vesicle formation in fibroblasts. *The Journal of Cell Biology*, 84(3):560–583, 1980.
- [81] P. Russell. Photonic crystal fibers. *Science*, 299(5605):358–362, 2003.
- [82] G. Donnert, J. Keller, C. A. Wurm, S. O. Rizzoli, V. Westphal, A. Schönle, R. Jahn, S. Jakobs, C. Eggeling, and S. W. Hell. Two-color far-field fluorescence nanoscopy. *Biophysical Journal*, page doi:10.1529/biophysj.107.104497, 2007.
- [83] A. M. Roccamo, M. F. Pediconi, E. Aztiria, L. Zanella, A. Wolstenholme, and F. J. Barrantes. Cells defective in sphingolipids biosynthesis express low amounts of muscle nicotinic acetylcholine receptor. *European Journal of Neuroscience*, 11(5):1615–1623, 1999.

- 
- [84] W. Stöber, A. Fink, and E. Bohn. Controlled growth of monosized silica spheres in the micron size range. *Journal of Colloid and Interface Science*, 26:62–69, 1968.

# A Appendix

## A.1 Imaging acetylcholine receptors

### A.1.1 Cell culture

CHO-K1/A5 cells were grown in Ham's F12 medium supplemented with 10% fetal bovine serum (FBS) for 2–4 days at 37 °C as in Ref. [83] before cytochemical experiments.

### A.1.2 Preparation of single plasma membrane sheets

For preparation of membrane sheets, CHO-K1/A5 cells were grown on polylysine-coated glass coverslips and disrupted by using a 300 ms ultrasound-pulse in ice-cold KGlu buffer (20 mM HEPES, pH 7.2, containing 120 mM potassium glutamate and 20 mM potassium acetate).

### A.1.3 Cholesterol depletion of cells and single plasma membrane sheets

CHO-K1/A5 cells and plasma membrane sheets, on the same coverslips, were treated with 10 mM methyl- $\beta$ -cyclodextrin (CDx; Sigma Chemical Co., USA) in KGlu-buffer for 20 min at 37 °C to deplete their cholesterol content.

## A.2 Miscellaneous

### A.2.1 PtK2 cell preparation for bleaching experiments

The PtK2 cells were grown on standard glass coverslips to a confluency of about 80 %. Fixation was carried out with cold methanol (-20°C) for 4 min. Immunostaining of microtubules was performed with anti- $\alpha$  Tubulin rabbit IgG (Abcam, Cambridge, UK) as primary antibody and with anti-rabbit conjugated Atto 532 IgG (Atto-Tec, Siegen, Germany) as secondary antibody, respectively, for 1h each at room temperature.

### A.2.2 Mowiol

6 g Glycerol AR (#4094, Merck, Darmstadt, Germany), 2.4 g Mowiol 4-88 (Hoechst, Germany), 6 ml water, 12 ml 0.2 M Tris pH 7.2 buffer

### A.2.3 Preparation of fluorescent nanoparticles

Silica nanoparticles doped with the fluorescent dye Atto 425 were prepared according to a modification of the Stöber method [84]. 0.5 mg of Atto 425 NHS and 3  $\mu$ l (about 9  $\times$  equivalents) of APS ([3-aminopropyl]triethoxysilane) were dissolved in 300  $\mu$ l of ethanol at room temperature. After 10 hours of stirring, the mixture was diluted with ethanol, and ammonium hydroxide (28 % in water) was added to a final concentration of 0.45 M. Then 110  $\mu$ l tetraethyl orthosilicate (TEOS) were added, yielding a molar ratio TOES/dye of approximately 500. The sample was then stirred overnight at room temperature. The reaction was stopped by diluting the mixture with two parts of solvent, and purified by three centrifugation/resuspension cycles.

## Acknowledgements

This work was performed in the department of NanoBiophotonics at the Max-Planck-Institute for Biophysical Chemistry in Göttingen. I thank everyone who directly or indirectly contributed to the success of this thesis.

Prof. Dr. Stefan W. Hell not only proposed the fascinating and challenging project of STED microscopy, but he has also provided an outstanding and inspiring scientific environment. His continuous input of new ideas and enthusiastic support has significantly contributed to the success of this work.

I would like to thank Prof. Dr. Josef Bille at the Kirchhoff Institute for Physics, University of Heidelberg, for his interest in this work and for being a referee of my thesis.

The sophisticated applications at the physical and technical limits were only possible with the collaborative help of highly dedicated experts:

- Prof. Dr. Stephan Siegrist, Dr. Tobias Rasse and Wernher Fouquet, European Neuroscience Institute Göttingen
- Prof. Dr. Francisco J. Barrantes and C. Javier Baier, UNESCO Chair of Biophysics & Molecular Neurobiology and Instituto de Investigaciones Bioquímicas, Bahía Blanca, Argentina

I also thank the following former and present members of the department of NanoBiophotonics:

- Dr. Katrin I. Willig and Dr. Marcus Dyba for their assistance during the initial stages.
- Dr. Andreas Schönle for valuable discussion and for help with his sophisticated “Inspector” software.
- Dr. Christian Eggeling for inspiring discussions.
- Dr. Jan Keller for valuable discussion, proof-reading and various calculation tools.
- Dr. Chaitanya Ullal for proof-reading and general support.
- Rebecca Medda for highly appreciated biological samples.
- Thorsten Staudt for special support in the microchip project.
- Brian Rankin for supportive assistance and proof-reading.
- Arnold Giske for valuable discussions and experimental advice.
- Mariano Bossi for preparing the important and versatile fluorescent beads.
- Gerald Donnert for assistance in the screening project.
- Miriam Schwentker for valuable discussions.
- Jaydev Jethwa and Harald Meyer for technical assistance.
- all the other members of the department for the creative and joyful environment.

This work would not have been possible without the great mechanical and optical workshop.

I especially thank my wife Corinna Kellner for always supporting and encouraging me throughout the past years. I also thank my parents Reinhardt and Petra Kellner, and parents-in-law Christian and Carola Pfeiffer for their support.

Göttingen, April 2007

## List of publications

Parts of this theses have been published as follows:

1. R. J. Kittel, C. Wichmann, T. M. Rasse, W. Fouquet, M. Schmidt, A. Schmidt, D. A. Wagh, C. Pawlu, R. R. Kellner, K. I. Willig, S. W. Hell, E. Buchner, M. Heckmann, S. J. Sigrist. Bruchpilot promotes active zone assembly, Ca<sup>2+</sup> channel clustering, and vesicle release. *Science* **312**, 1051–1054 (2006).
2. K. I. Willig, R. R. Kellner, R. Medda, B. Hein, S. Jakobs, S. W. Hell. Nanoscale resolution in GFP-based microscopy. *Nature Methods* **3** (9), 721–723 (2006).
3. R. R. Kellner, C. J. Baier, K. I. Willig, S. W. Hell, F. J. Barrantes. Nanoscale organization of nicotinic acetylcholine receptors revealed by stimulated emission depletion microscopy. *Neuroscience* **144** (1), 135–143 (2007).